Effects of orbital evolution on lunar ice stability

Matthew A. Siegler,[1] Bruce G. Bills,[2] and David A. Paige[1]

Received 13 May 2010; revised 19 November 2010; accepted 10 January 2011; published 31 March 2011.

[1] Many regions near the lunar poles are currently cold enough that surface water ice would be stable against sublimation losses for billions of years. However, most of these environments are currently too cold to efficiently drive ice downward by thermal diffusion, leaving impact burial as the primary means of protection from surface loss processes. In this respect, most of the present near-surface thermal environments on the Moon may actually be quite poor traps for water ice. This was not always the case. Long-term orbital changes have dramatically altered the lunar polar thermal environment. We develop a simple model of the evolution of the lunar orbit and spin axis to examine the thermal environments available for volatile deposition and retention in the past. Our calculations show that some early lunar polar environments were in the right temperature regime to have collected subsurface ice if a supply were available. However, a high-obliquity period, which occurred when the Moon was at about half its present distance from the Earth, would either have driven this ice out into space or deep into the lunar subsurface. Since that time, as the lunar obliquity has slowly decreased to its present value, environments have undergone their own thermal evolution, and each of the current cold traps experienced a period when they were most efficient at thermally burying ice. We examine the thermal history of a lunar polar crater to provide a framework for examining other processes effecting volatiles in the Moon's near-surface cold traps.

Citation: Siegler, M. A., B. G. Bills, and D. A. Paige (2011), Effects of orbital evolution on lunar ice stability, *J. Geophys. Res.*, *116*, E03010, doi:10.1029/2010JE003652.

1. Introduction

[2] The lunar spin axis is nearly perpendicular to the ecliptic and as a result, there are regions on the floors of polar craters, and near other topographic features, that do not see direct Sunlight. However, this has not always been the case. The past orientation of the lunar orbit and spin axes created a very different illumination environment at the poles. The objective of this study is to examine the effect of the outward tidal evolution of the lunar orbit upon surface and shallow subsurface temperatures near the lunar poles. The most dramatic period in the Moon's orbital evolution was an episode of high obliquity, the Cassini state transition, which occurred when the Moon was at roughly half its current distance from the Earth. During that episode, as identified by *Ward* [1975], the polar regions were very well illuminated. It has generally been assumed that this illumination event was sufficient to remove all volatiles from the lunar polar surface region, and that shadowed regions have slowly collected ice since [*Arnold*, 1979]. However, no detailed models of the surface and subsurface temperature response to the past lunar orbital evolution and resulting insolation history have been presented.

[3] The recent detections of water and water ice on the Moon have opened a new chapter in lunar science [*Feldman et al.*, 2001; *Pieters et al.*, 2009; *Clark*, 2009; *Sunshine et al.*, 2009; *Colaprete et al.*, 2010]. The question of whether ice is present has been replaced by questions of ice quantity, origin, and longevity. In an effort to address these new questions, which are dominantly controlled by temperature, we build a thermal framework within which depositional and loss processes can be examined. We outline a thermal history of environments capable of capturing and preserving ice over the evolution of the lunar orbit. A single crater, modeled to approximate Shackleton (at 89.7°S, 111°W), is examined to describe general trends of evolution of temperatures through time, though spatial variation around the lunar pole should be expected.

[4] The survival of water ice in shadowed polar craters was suggested by *Urey* [1952] and first examined in detail by *Watson et al.* [1961a, 1961b]. Due to the small angle between the lunar spin axis and the ecliptic normal (1.54°), surface temperatures within polar craters can remain cold enough to prevent substantial loss of ice by sublimation. The temperature of 100 K (more precisely 101.35 K) has been traditionally used to define lunar cold traps since the sublimation rate of exposed water ice will slow to roughly 10^{-9} kg m^{-2} yr^{-1}, or about 1 mm Gyr^{-1}, preserving ice over

[1] Earth and Space Sciences, University of California, Los Angeles, California, USA.
[2] NASA Jet Propulsion Laboratory, Pasadena, California, USA.

0148-0227/11/2010JE003652

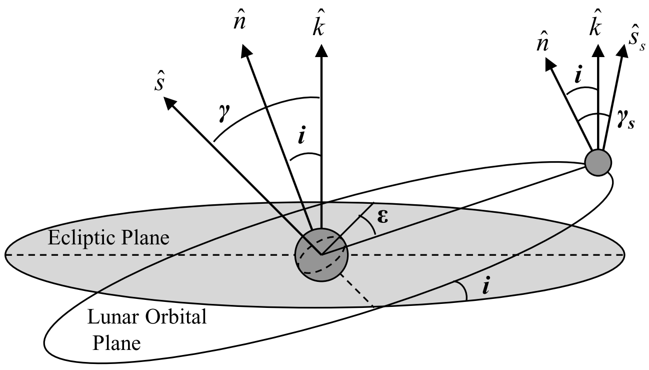

Figure 1. Definitions of vectors $\hat{k}$ (ecliptic normal), $\hat{n}$ (the Moon's orbit normal), and $\hat{s}$ (Earth's spin axis) and orbital angles ε (inclination of Earth's equator to the Moon's orbit), i (inclination of the Moon's orbit to the ecliptic), and γ (obliquity of Earth's equator to the ecliptic). Note $\hat{s}$ is the vector of the Earth spin axis, not the Moon as presented later as $\hat{s}_s$; likewise, γ_s is the Moon's obliquity.

geologic time scales [*Watson et al.*, 1961a, 1961b; *Vasavada et al.*, 1999; *Schorghofer and Taylor*, 2007].

[5] Although the illumination of a planet is affected only by obliquity, moons depend on the convolution of orbital inclination and obliquity, referred to here as *solar declination* or θ_{max} (as shorthand for the maximum yearly declination, or subsolar latitude, of the Sun). The current θ_{max} represents the difference between the lunar orbital inclination (5.15°) and obliquity (of the lunar spin axis to the lunar orbit normal, 6.69°). This 1.54° angle between the ecliptic plane and the lunar equator essentially means that a hill or crater wall rising 1.54° above the horizon will shadow a viewer at the lunar pole.

[6] Both inclination and obliquity have changed with time as the Moon evolved outward in its orbit. Past lunar orbital inclination varied greatly in the early lunar history [*Goldreich*, 1966]. About halfway through the Moon's outward evolution, a large change in obliquity occurred due to a transition in the lunar Cassini state [*Peale*, 1969; *Ward*, 1975; *Arnold*, 1979]. Prior studies have assumed that all near-surface volatiles were lost to space during this transition and any present polar volatiles would have accumulated steadily over the past 2 to 3 billion years since [*Arnold*, 1979].

[7] Here we revisit that assumption and examine if past orbital and rotational variations may have been able to drive early ice (and other volatiles) from the lunar surface into the subsurface. This paper will redevelop a history of the lunar orbit and spin, examine how this history determined the insolation within a near-polar lunar crater (based on Shackleton: 89.7°S, 111°W), and how this radiative forcing influenced surface and subsurface temperatures. This single crater is meant as a guide in understanding the temporal effect of lunar orbital evolution on cold trap temperatures, but does not represent the history of temperatures in the broader polar region. Shackleton's proximity to the lunar south pole does however make it one of the first craters to become permanently shadowed after the Cassini state transition. Further work is in process to examine the thermal evolution of the entire polar near surface (as in the work of *Paige et al.* [2010]). We will also briefly address the likely effects of this thermal history on migration of water vapor through the subsurface, but a full discussion of diffusion processes is beyond the scope of this study.

2. Lunar Orbital History

[8] The maximum latitudinal excursion, away from the equator, to which the subsolar point on the Moon can go, denoted here by $\theta_{max,}$ is a convolution of two angles, the first is that between the Moon's orbit normal and the ecliptic normal (here called "inclination"), and the second is that between the Moon's spin axis and the lunar orbit normal ("obliquity" in this text). Inclination is not affected by the lunar obliquity, but obliquity variations are a direct response to the instantaneous orbital inclination. Therefore, we need first to calculate the lunar inclination history, and then examine its effect on lunar obliquity. Inclination is often denoted $i = \cos^{-1}(\hat{n}\cdot\hat{k})$, and obliquity $\gamma = \cos^{-1}(\hat{n}\cdot\hat{s}_s)$ where $\hat{n}$, $\hat{s}_s$, and $\hat{k}$ are unit vectors along the satellite orbit normal, spin axis (subscript "s" denoting satellite versus planet), and ecliptic normal (Figure 1).

[9] The torques which drive the variation of these angles are related to the lunar semimajor axis. However, the time evolution of lunar semimajor axis is not well constrained, as it depends upon unknown rates of dissipation within the Earth-ocean system which drive the Moon to move outward. Approximations of outward lunar migration can be made [*Bills and Ray*, 1999], but we do not attempt that in this paper. Instead, we examine the insolation environment as a function of Earth-Moon separation distance. As a general reference, the Cassini transition is likely to have occurred between 3 to 4 billion years ago. It should also be noted here that this model does not include any possible reorientation of the lunar surface due to large impacts or true polar wander.

2.1. Inclination History

[10] Inclination variations are a direct response to torques from the Sun (which cause the lunar orbit to precess about the ecliptic) and torques from the oblate body of the Earth (which cause the lunar orbit to precess about the Earth's equatorial plane). The relative magnitude of these torques depends on the lunar semimajor axis.

[11] A method to numerically integrate the torques upon the lunar orbit was developed by *Goldreich* [1966] and revisited by *Touma and Wisdom* [1994], *Atobe and Ida* [2007], and others. Here we also calculate the lunar orbital precession and inclination history based on the Goldreich model. All calculations here assume, as in the work of *Goldreich* [1966], circular orbits for the Earth and Moon, so nodal precession is important, but apsidal precession is ignored.

[12] As the diurnal cycle (the month of a given past era) has always been much shorter than precessional time scales the Moon is treated as a ring of material subject to torques from the oblate Earth and from the Sun. Torques from the Sun will cause this ring to precess about the ecliptic while torques from the oblate Earth will cause it to precess about the Earth's equatorial plane. In the early lunar history, when the lunar semimajor axis was much smaller, torques from the oblate Earth on this ring played a larger role in Moon's

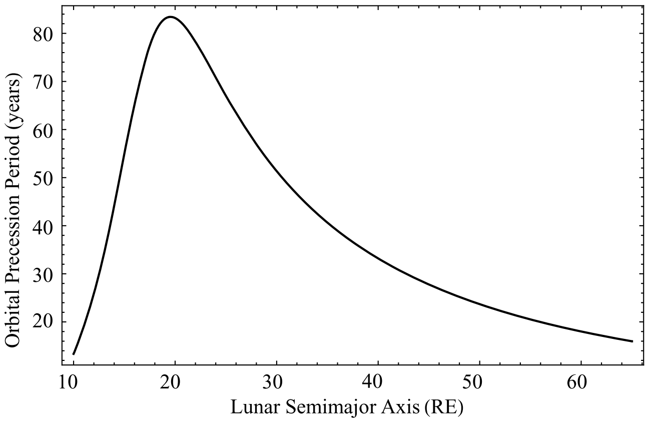

Figure 2. Lunar nodal precession period as a function of semimajor axis [adapted from *Touma and Wisdom*, 1994]. Currently ~18.6 years but as long as ~80 years at about 20 RE.

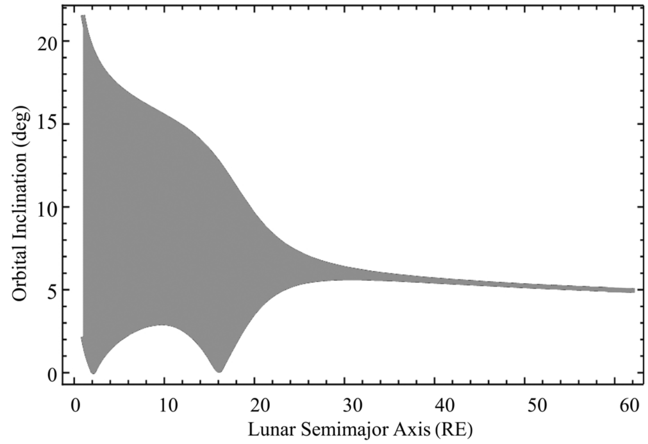

Figure 3. Inclination of the lunar orbit versus semimajor axis for Darwin-Kaula-Goldreich tides adapted from *Touma and Wisdom* [1994]; the filled section represents rapid precessional time scale oscillation. This angle is currently about 5.15°.

orbital motion than it does currently. This caused the lunar orbital plane to precess about both the ecliptic and Earth's equatorial plane ($\hat{n}$ precessed about $\hat{s}$). Simultaneously, the Earth's equatorial plane was also varying dramatically about the ecliptic ($\hat{s}$ precessed about $\hat{k}$). This resulted in large inclination variations on precessional time scale (currently 18.6 years, but as long as 80 years in the past, see Figure 2).

[13] As the lunar semimajor axis grew and the oblate Earth acted more like a gravitational point source, solar torques began to dominate the Moon's motion. This outward evolution drove the orbit to the nearly constant inclination to the ecliptic seen today (where $\hat{n}$ precesses about $\hat{k}$) [*Goldreich*, 1966]. The resulting calculation for a constant and equal phase lag in the Earth's tides (Darwin-Kaula-Goldreich tides [*Darwin*, 1880]) from *Touma and Wisdom* [1994] is shown in Figure 3.

2.2. Obliquity History

[14] Obliquity variations result from the fact that the spin axis precesses about the instantaneous orbit normal and damps toward it ($\hat{s}_s$ precesses about *and* damps toward $\hat{n}$). For a nonprecessing orbit, damping within the satellite would lead it to have zero obliquity. However, if the orbit is constantly precessing ($\hat{n}$ about $\hat{k}$), the spin axis lags with a predictable angle determined by the lunar moments of inertia and the ratios of the spin and orbit precession rates: a Cassini state. As the orbital precession rate changes, the Cassini state "lag angle" (this angle is obliquity when referenced to the orbital plane, $\theta_{\max}$ when referenced to the ecliptic) changes accordingly.

[15] This spin-orbit relation, first identified 1693 by G.D. Cassini, was first given a proper dynamical basis in work by *Colombo* [1966] and *Peale* [1969]. A Cassini state is an outcome of dissipation within a satellite. Internal dissipation will be minimized within the satellite when the motion of the parent body in the sky is minimized. This occurs when the satellite spin axis precesses about its orbit normal in the same period as the orbit normal precesses about the ecliptic normal, causing these two vectors to lie in a single plane (or line when viewed from above the ecliptic plane, as in Figure 4).

[16] *Peale* [1969] identified that the spin axis, orbit normal and ecliptic normal can only maintain the required coplainarity in four specific obliquity states (four different, evolving "lag angles"). Peale showed that one of these states is unstable (state 4) and that only 2 of these states (states 2 and 3) remain throughout the entire evolution of the lunar orbit. One of the remaining states is retrograde (state 3), leaving the Moon to currently reside in state 2. The prograde states are illustrated in Figure 5, similar to *Ward* [1975].

[17] In Ward's model, the Moon is assumed to have formed in the lowest obliquity of the four possible states (state 1). This argument has merit as all other known planetary bodies (including Mercury) locked in a Cassini state lie in state 1, having lacked the semimajor axis evolution of the Moon. This would also be a likely outcome of a Moon formed from an impact created ring of material about the early Earth. As the lunar semimajor axis grew, the orbit precession rate varied according to the changing torques

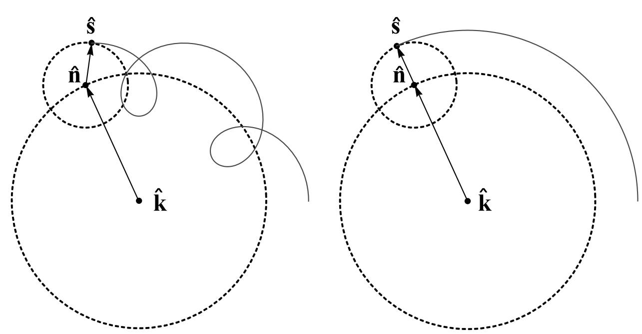

Figure 4. In a generalized Cassini state, the spin axis precesses about its orbit normal in the same period as the orbit normal precesses about the ecliptic normal. This is depicted as viewed from above the ecliptic plane in (left) a Cassini state and (right) not a Cassini state. The line connecting the two points is referred to here as the Cassini plane.

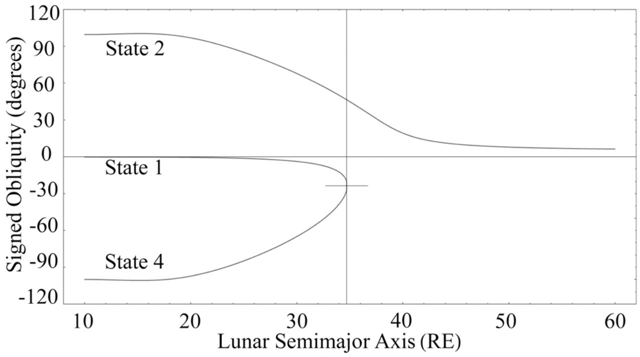

Figure 5. The three prograde obliquity states as in the work of *Ward* [1975] projected onto the Cassini plane. Negative obliquity refers to whether the spin axis and ecliptic normal lie on the same side (+) or opposite sides (−) of the orbit normal, not to a "flipping" of the Moon. Both *Ward* [1975] and this paper assume the Moon formed in state 1 then transitioned to state 2 upon the disappearance of state 1.

(Figure 2). The evolving lunar orbit caused the obliquity to grow until state 1 and state 4 merged into a single state, and then ceased to exist. Since this transition only one of the remaining states (state 2) is prograde and therefore the current one [*Peale*, 1969]. During this Cassini transition the Moon briefly went to a very high obliquity which undoubtedly impacted the polar thermal environment [*Ward*, 1975].

[18] The actual Earth-Moon distance at which the Cassini transition occurred depends on the past lunar moments of inertia [*Bills et al.*, 2010]. As the current lunar shape is far from hydrostatic, past lunar moments of inertia are even more difficult to determine. *Garrick-Bethell et al.* [2006] gave evidence the current shape may have frozen in as an early 3:2 spin-orbit resonance, but did not rule out other origins of the current lunar shape. The reorientation of the Moon during the Cassini state transition will itself drive a reshaping of the Moon [*Bills et al.*, 2010].

[19] The length of time required for the Cassini transition is also uncertain as it depends on dissipation within the Moon. Having assumed a perfectly dissipative Moon for his calculations, *Ward* [1975] suggests motion during the transition follows an adiabatic invariant (illustrated in Figure 7b). This results in a maximum obliquity of 77° damping from state 1 to 2 in the order of 10^5 years.

[20] We chose to pursue a simplified numerical integration of the damped lunar spin axis precession. For a synchronously rotating, low-eccentricity body, one can approximately equate the rate of change in the spin angular momentum and applied gravitational torque to give [*Ward*, 1973, 1992; *Kinoshita*, 1977; *Bills and Comstock*, 2005, *Bills*, 2005; *Hilton*, 1991]

$$\frac{d\hat{s}_s}{dt} = (\alpha(\hat{n}\cdot\hat{s}_s) + \beta)\,(\hat{s}_s \times \hat{n}) - \gamma(\hat{n} - \hat{s}_s(\hat{n}\cdot\hat{s}_s)) \qquad (1)$$

where, $\hat{s}_s$ and $\hat{n}$ are unit vectors along the satellite spin axis and orbit normal, respectively, while α and β scalar rate parameters related to departure from spherical symmetry of the rotating body, and γ is a dissipative rate parameter which tends to drive the spin pole toward the orbit pole. Parameters α and β, depend on the principal moments of inertia (where $A < B < C$), via (corrected from *Bills and Comstock* [2005] and *Bills* [2005])

$$\alpha = -\frac{3}{2}n\left(\frac{4C - B - 3A}{4C}\right) \text{ and } \beta = -\frac{3}{2}n\left(\frac{B - A}{4C}\right) \qquad (2)$$

with n the orbital mean motion or mean angular rate. For the actual Moon, every variable in equation (1) is evolving in time. Values for the spin rate and orbital mean motion come from the inclination integration discussed in section 2.1.

[21] The integration of this torque balance allows for evolving lunar shapes, dissipation, and orbital histories that are uncertain and beyond the scope of this paper [*Bills et al.*, 2010]. As the current Moon is not hydrostatic, we chose to use a lunar shape model which assumes the current lunar moments of inertia to be a combination of a hydrostatic and frozen in component. We then evolved the hydrostatic component backward as it would vary with semimajor axis. This differs from *Ward* [1975], who used the current lunar moments of inertia, and other authors who freeze in the current lunar shape early on [*Wisdom*, 2006; *Garrick-Bethell et al.*, 2006]. Figure 6 illustrates two possible variations in the semimajor axis of the Cassini transition resulting from our calculations. We find the roughly 77° maximum obliquity to be robust despite other orbital changes.

2.3. The θ_{max} History

[22] Insolation upon the lunar surface depends neither on inclination or obliquity alone, but on their convolution, θ_{max}. θ_{max} denotes the amplitude of yearly subsolar latitude variations about the equator. This angle is mathematically $\cos^{-1}(\hat{s}_s \cdot \hat{k})$ and is obtained by projecting the spin axis onto the ecliptic plane. For the inclination and obliquity histories presented above, the resulting θ_{max} is shown in Figure 8. For

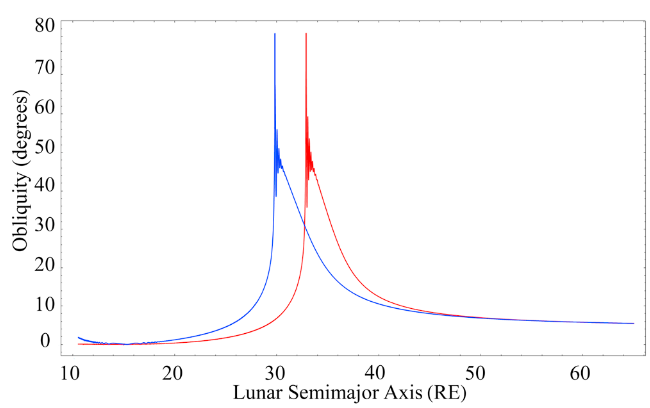

Figure 6. Numerically integrated obliquity as a lunar semimajor axis (absolute value). The blue line illustrates a nonevolving lunar shape, as in Figure 5 (as in the work of *Ward* [1975] or *Garrick-Bethell et al.* [2006]); the red line illustrates our partial hydrostatic evolution. This angle is currently about 6.69°. We approximate the Cassini state transition as 34.2 RE (red for *Ward* [1975]) and 30 RE (blue for this paper).

a brief time during the Cassini state transition, the maximum θ_{max} reached about 82.9° (77° obliquity + 5.9° inclination, Figure 7), in agreement with *Ward* [1975].

[23] Due to the early inclination variations, the θ_{max} varied greatly on precessional time scale (Figure 2). For instance, at about 15 RE (semimajor axis in Earth Radii) θ_{max} varied from roughly 1 to 14° over each 54.8 year precession cycle.

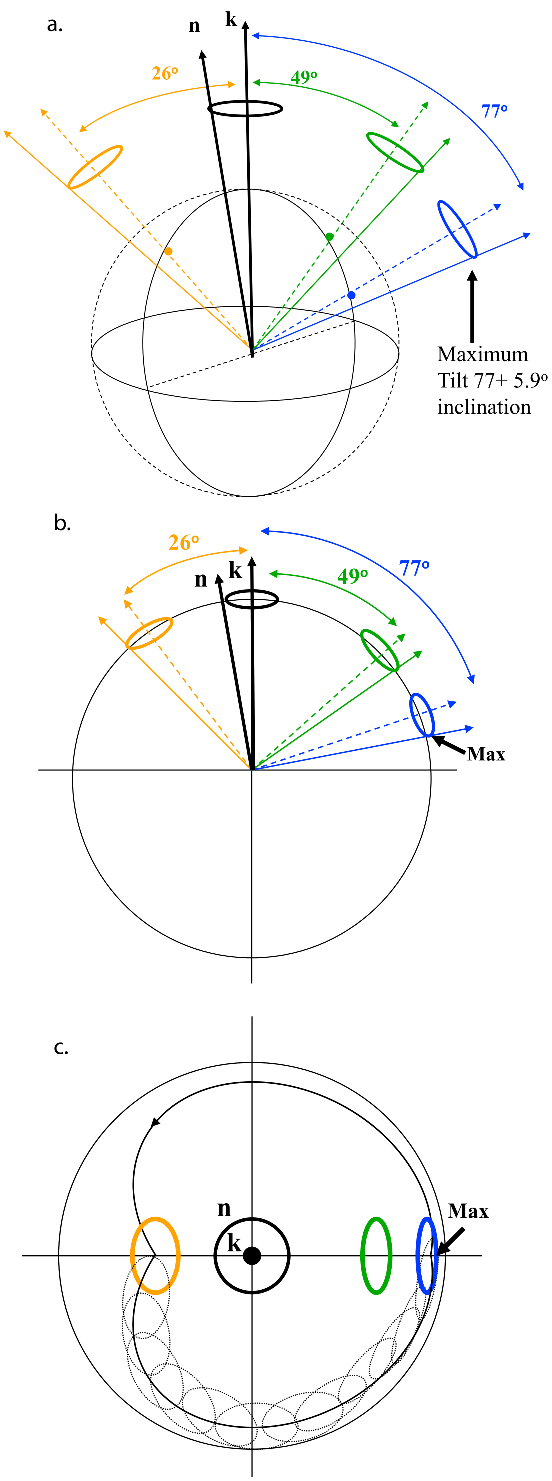

[24] As the semimajor axis grew, Cassini state 1 drove the Moon to a higher obliquity. Simultaneously, due to the handoff from Earth dominated orbital precession to solar dominated precession, inclination variations began to die down after about 17 RE. This caused θ_{max} to slowly increase over the time scale of orbital evolution, but remain relatively constant over the precession time scale.

[25] During the Cassini state transition itself, when states 1 and 4 merge and vanish, the lunar spin axis is not in any Cassini state. The spin axis, having left Cassini state 1, will spiral out of the Cassini plane. Continuing on its initial trajectory, the spin axis will reach a maximum obliquity of ~77° [*Ward*, 1975]. Dissipation within the Moon will drive the spin axis along a spiral which damps into Cassini state 2.

[26] When projected on the ecliptic (Figure 7c), the transitioning spin axis follows a trajectory on the orbit plane which itself is precessing. This results in θ_{max} following a small epicycle with a radius equal to the instantaneous orbital inclination (about 5.9° at our transition point of 30 RE). Therefore the maximum θ_{max} will be about 77° + 5.9° = 82.9°. However, θ_{max} will dip to 77° −5.9° = 71.1° on the same precessional cycle (a 51.4 year period at 30 RE).

[27] The spin pole continues to spiral (in kidney shaped paths when viewed from above as illustrated in Figure 7c) for a few 10^5 years [*Ward*, 1975], depending on dissipation within the Moon. As each of these kidney-shaped loops takes >10^3 years, the spin axis will experience many periods with a θ_{max} near the 82.9° maximum.

[28] Once these oscillations have damped, the spin axis will settle into a new stable state in the one remaining prograde Cassini state, state 2, with an obliquity of about 49° (and θ_{max} of 54.9°). Following the trajectory implied by state 2, the θ_{max} will be simply derived as obliquity minus orbital inclination (e.g., the current 1.54° = 6.69°–5.15°). The resulting history of θ_{max}, or amplitude of the yearly oscillation of the subsolar point about the equator, is illustrated in Figure 8. As in Figure 3, the width of the filled section illustrates the variation of this angle over a single precession cycle at the given semimajor axis (with period given in Figure 2).

3. Surface Radiative History

[29] The current 1.54° θ_{max} leads to the possibility that near polar craters can remain in persistent shadow. However, due to the dramatic changes in this angle described above, no lunar crater created before the Moon reached roughly 32 Earth radii semimajor axis has been in truly

Figure 7. Cartoon of Cassini state transition viewed looking at (a) perspective view, (b) the cross section along the Cassini plane, and (c) from above the ecliptic (note *Ward* [1975] projects on the lunar orbit plane). "Max" denotes the maximum θ_{max} angle of 82.9°. The ellipses denote the path of the spin axis over a single precession cycle (orange illustrates the path of the spin axis pointing just before the transition, the blue at the peak obliquity of the transition, green at the end of the transition; the gray in Figure 7c illustrate the "epicycles" traveled along the shrinking kidney-shaped path as the spin axis slowly migrates to state 2 over 10^5–10^6 years [*Ward*, 1975]).

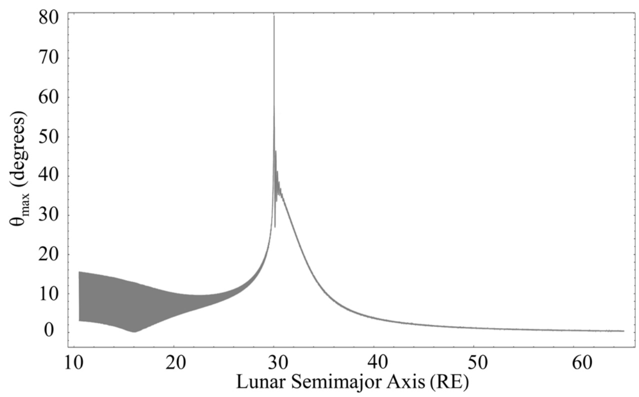

Figure 8. Modeled lunar θ_{max} as a function of lunar semimajor axis. This angle represents the amplitude of subsolar point variations about the equator. The filled section represents rapid precessional time scale oscillation (period length given in Figure 2). This angle is currently about 1.54°.

permanent shadow. For a given latitude, size, and topography, each crater has its own history of direct and reflected illumination.

[30] We can divide the insolation history into three distinct periods: (1) an early period of large inclination driven variations, (2) a middle period of high obliquity due to the Cassini state transition, and (3) the current period of relatively low θ_{max}.

[31] The early lunar orbital plane varied dramatically over the nodal precession period (18.6 years currently, 80 years at its longest, Figure 2). This is illustrated in the filled section of the curve prior to 30 RE in Figure 3. This caused θ_{max} to also change dramatically on this time scale creating early precession period length "seasons" on top of the yearly seasons (the filled section of the curve on Figure 8). As the semimajor axis grew, inclination variations lessened and these precession length seasonal effects essentially disappeared.

[32] Subsolar longitude varies each diurnal period at a rate depending on the lunar spin rate. Assuming a 1:1 spin-orbit resonance was established early on, this spin rate can be found from Kepler's 3rd law. The current solar diurnal period (draconic month) on the Moon is 29.53 days, having increased from about 1.86 days ("day" here means our current 24 h day) when the Moon was at 10 RE semimajor axis. Possible early nonsynchronous orbits could have given different length diurnal periods, however diurnal modulations are a relatively minor effect near the poles where insolation variations are dominated by yearly and precessional cycles.

[33] Yearly cycles cause an oscillation of the subsolar latitude to $\pm\theta_{max}$. Due to the precession of the lunar orbit, the length of the lunar yearly cycle is shorter than an Earth year. The frequency of effective lunar year (or draconic year) is a sum of 2π/precession period and 2π/365.25 days. This current effective lunar year is about 346 days and was closer to a year in length in the past (with a maximum of 361 days at about 20 RE). Precessional cycles in θ_{max} result in larger effects on the polar insolation.

[34] These cycles equate to a movement subsolar latitude and longitude. Using these values we now develop a simple system to calculate the instantaneous illumination of a cratered spherical body.

3.1. Flat Surface Insolation

[35] The instantaneous insolation on a spherical body can be written as

$$F = S(1 - A) \parallel \cos\gamma \parallel \tag{3}$$

where S is the solar flux at 1 AU (1370 W m^{-2} currently), A is the solar albedo and

$$\parallel \cos\gamma \parallel = \frac{[|(\cos\gamma)| + \cos(\gamma)]}{2} = \frac{[|(u \cdot u_{ss})| + (u \cdot u_{ss})]}{2} \tag{4}$$

where the double vertical lines denote the "clipped" value, $\|x\| = \frac{x-|x|}{2}$ and $|x|$ is the absolute value of x. Here u_{ss} and u are unit vectors from the center of the Moon to the subsolar point and the point of interest, explicitly

$$u = \{\cos\theta\cos\phi, \cos\theta\sin\phi, \sin\theta\} \tag{5}$$

$$u_{ss} = \{\cos\theta_{ss}\cos\phi_{ss}, \cos\theta_{ss}\sin\phi_{ss}, \sin\theta_{ss}\} \tag{6}$$

so

$$\cos\gamma = u \cdot u_{ss} = \sin\lambda\sin\theta_{ss} + \cos\theta\cos\theta_{ss}\cos(\phi - \phi_{ss}) \tag{7}$$

where θ and ϕ are latitude and longitude, the subscript "ss" means subsolar (so θ_{ss} is subsolar latitude to be consistent with our θ_{max} notation) [*Ward*, 1974].

[36] The subsolar longitude cycles from 0 to 2π each draconic month (29.53 days currently), which is calculated as the inverse of the sum of the frequency calculated from Kepler's 3rd law (2π/27.3 days) for a synchronous orbit and 2π/365.25 days. Insolation is clipped to zero when the Sun sets below the local horizon (which may change when in a crater (see section 3.2).

[37] The subsolar latitude is modulated by the amplitude of θ_{max} (Figure 8). Most compactly (ignoring phase) subsolar latitude can be written as

$$\theta_{ss} = \left(B + C\cos\omega_{pre}t\right)\sin\omega_{year}t \tag{8}$$

where ω_{pre} and ω_{year} are 2π/(precession period) and 2π/(year), B is the mean value θ_{max} over a precession cycle and C is the amplitude of the variation of θ_{max} on the precessional time scale (half width of the line in Figure 8).

[38] The blue curves in Figure 9 illustrates the illumination on a flat surface at 89.7°S (the current location of Shackleton crater) at 15 RE semimajor axis (when mean θ_{max}, B = 7.17 and amplitude, C = 6.2, solar constant, S = 1370 W m^{-2} and a precession period of about 54.8 years). Being at high latitude alone reduces the solar power reaching the surface to about 1/4 and causes a half year long polar night. The large inclination variations (Figures 3 and 8) cause modulations of the yearly maximum illumination. Diurnal modulations (only 3.41 days at 15 RE semimajor axis) cause only a minor variation (apparent in Figure 9b).

[39] The illumination of a sloped surface is given by

$$F_{sloped} = S(1 - A) \parallel \cos\Lambda \parallel \tag{9}$$

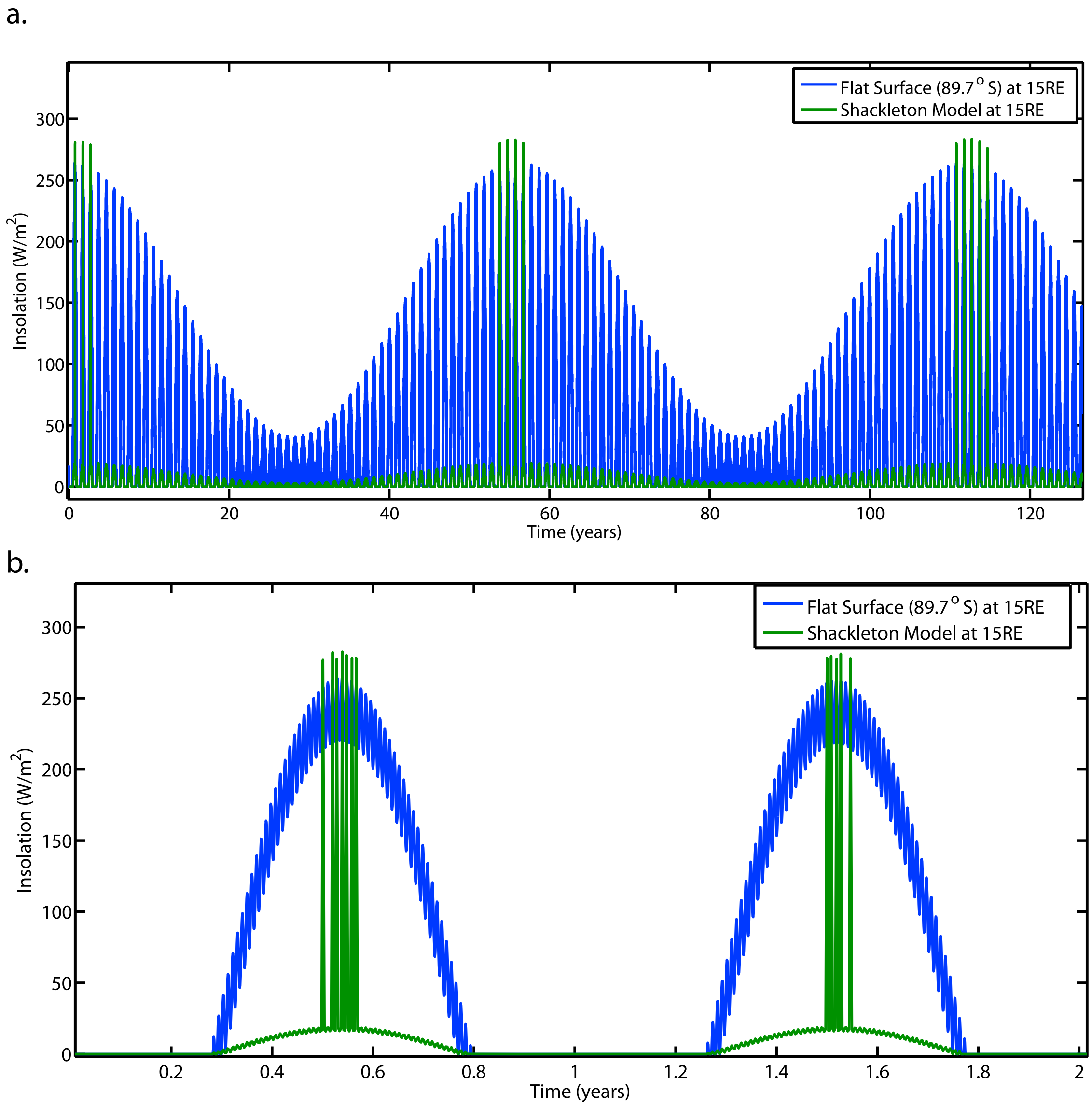

Figure 9. Insolation for a hypothetical flat surface at 89.7°S latitude (blue) and for a point at the center of Shackleton crater (green) when the Moon had a semimajor axis of 15 RE for (a) two precession cycles and (b) 2 years. Note 6 month darkness and 3.4 day long diurnal period in Figure 9b and the brief periods of direct illumination once per precession cycle.

with

$$\cos \Lambda = \cos(v)\sin(90^\circ - \gamma) + \sin(v)\cos(90^\circ - \gamma)\sin(w - \phi) \quad (10)$$

where v is the slope angle, $(90^\circ - \gamma)$ is the Sun elevation angle, and w is the azimuth of the gradient (degrees east of the local meridian line) [*Kimball and Hand*, 1922; *Kimball*, 1925]. Slopes amplify the diurnal variations in illumination since they receive higher-angle light for half the diurnal period and lower-angle light for the other half.

3.2. Crater Insolation

[40] In near-polar craters illumination cycles can have an even larger effect. For example, a crater wall might shade its interior for most of a precession cycle, but then allow a few years of direct insolation. To estimate temperatures in near polar craters we adapt an insolation model from *Ingersoll et al.* [1992], *Svitek* [1992], and *Buhl et al.* [1968]. This model assumes craters to be sections of a sphere and all visible reflection and infrared reradiation to be isotropic (Lambertian). The diameter to depth ratio of this spherical section is determined by a survey of typical lunar craters [*Pike*, 1974, 1977]. For craters greater than about 15 km in diameter, a *diameter to depth* ratio D = $(\text{diameter})^{(0.7)}$ was found to approximate most bowl shaped craters (about 2.5 km deep for a 20 km crater) [*Ingersoll et al.*, 1992].

[41] In this paper we apply this model to Shackleton crater (modeled as 20 km diameter at 89.7°S, 111°E). Shackleton was chosen for its proximity to the lunar south pole, but with an estimated age of 3.6 Gyr [*Spudis et al.*, 2008] it may not even have formed until after the Cassini transition.

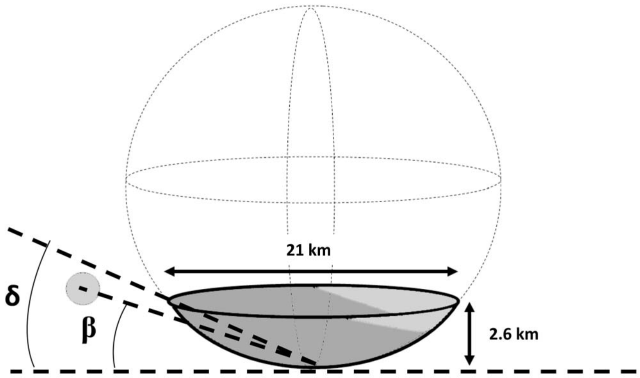

Figure 10. Shackleton crater insolation model adapted from *Ingersoll et al.* [1992], diameter *Haruyama et al.* [2008], depth fit to Diviner data (D = 8). The Sun (the gray circle) is assumed to be a point object, so if the local Sun angle β is below the angle to the rim δ, F_c is used for the incident radiation.

Shackleton was found by the Selene mission to be deeper than the average crater (with D = 5) and was found to have an atypical truncated cone shape [*Haruyama et al.*, 2008]. However, as discussed in section 4.1, an analytical bowl shaped model with D = 8 (or roughly 2.6 km depth) was found to agree more closely with temperature measurements of Shackleton from the Diviner Lunar Radiometer. This highlights the limiting ability of an analytical bowl shaped crater to approximate an irregular crater. For consistency with available data and future literature [*Paige et al.*, 2010], D = 8 was adopted throughout this paper. Figure 10 shows our model for Shackleton crater.

[42] The flux entering the area circumscribed by the crater rim is modeled to be scattered equally throughout the crater due to its spherical geometry and Lambertian surface. Discrepancy between data and model might also be diagnostic of a need for non-Lambertian scattering and reradiation, subsumed here in the artificial diameter to depth ratio. Given these properties, the total visible and infrared flux reaching a shadowed section can be approximated

$$F_c = S\frac{4\varepsilon(1-A)}{D^2}\left(1+\frac{A}{\varepsilon}\right)|\cos\gamma| \tag{11}$$

where ε is the surface thermal emissivity [*Ingersoll et al.*, 1992]. A crater with a tilted rim can be simulated by replacing $\cos\gamma$ with $\cos\Lambda$ (equation (10)).

[43] In our simplified model, $F + F_c$ is used when a point is directly illuminated, and F_c when it is in shadow. The Sun is assumed to be a point object, so if the local Sun angle, γ (or Λ for a tilted crater rim), is below the angle to the rim δ, F_c is used for the incident radiation. For a point at the center of a crater at latitude θ_{crater}, δ is defined

$$\delta = \tan^{-1}\left(\frac{2}{D}\right) \tag{12}$$

For Shackleton crater (D = 8) this means the center of the crater floor remains in permanent shadow until the Sun rises 14.04° above the horizon. The resulting calculated insolation at the center of our modeled Shackleton crater at 15 RE semimajor axis is shown in Figures 9a and 9b.

4. Near-Surface Thermal Model

4.1. Thermal Model: Introduction

[44] In creating a thermal model of the distant lunar past, we must make several assumptions. Here we assume the lunar regolith density structure has not changed despite billions of years of meteorite bombardment. We also assume the heat flow from radioactive sources and tidal heating within the Moon to be constant (estimates can be found in the work of *Peale and Cassen* [1978]). Furthermore, the solar flux is held constant (even though it is likely to have increased by 30% over the past 4.5 Gyr) [*Sackmann et al.*, 1993]. The Moon is also assumed to have not undergone any true polar wander or reorientation by large impacts. These assumptions are difficult to bypass as they are uncertain and tied to time, while our orbit model is tied to lunar semimajor axis. Without knowing the rate of lunar orbital recession, we cannot accurately estimate how these variables evolved.

[45] The surface temperature balance for any given location was calculated numerically with an explicit finite difference, 1-D, layered thermal model similar to that described by *Keihm* [1984], *Vasavada et al.* [1999], and *Leighton and Murray* [1966]. These models balance heat into the system from incident radiation, with heat lost due to infrared emission and conduction into the subsurface. Explicitly, the surface heat balance can be written

$$Q_{in} - Q_{out} = 0 = F - \varepsilon\sigma T^4 - k\frac{\partial T}{dz} \tag{13}$$

with F as the absorbed insolation (equation (3), F, or 14, F_c), ε the infrared emissivity, σ Boltzmann's constant, and k thermal conductivity of the surface layer. Calculations here use a 23% solar albedo [*Haruyama et al.*, 2008] and emissivity of 0.95 [*Vasavada et al.*, 1999].

[46] As the solution for temperature depends on the near-surface gradient (dT/dz), subsurface thermal properties also affect the surface temperature. This gradient is solved with a 1-D thermal diffusion model and assumed subsurface thermal properties. From subsurface temperature measurements of the Apollo 15 and 17 heat flow experiments it is clear that assignment of thermal properties is crucial for model accuracy. For instance, the Apollo 15 experiment showed an increase in mean temperature of 45 K within the top 35 cm due to the low density and strongly temperature-dependent properties of the lunar regolith.

[47] We adopt the thermal properties model found to match the Apollo heat flow experiment [*Keihm*, 1984]. This model has a surface layer density 1250 kg m^{-3} atop layers increasing to 1900 kg m^{-3} (equation (14)). The models used here follow the Apollo 15 fit with surface layer thickness, z_s, of 2 cm, and *e*-folding, z_e depth of 4 cm.

[48] A temperature-dependent thermal conductivity was used (the effective conductivity including radiation between

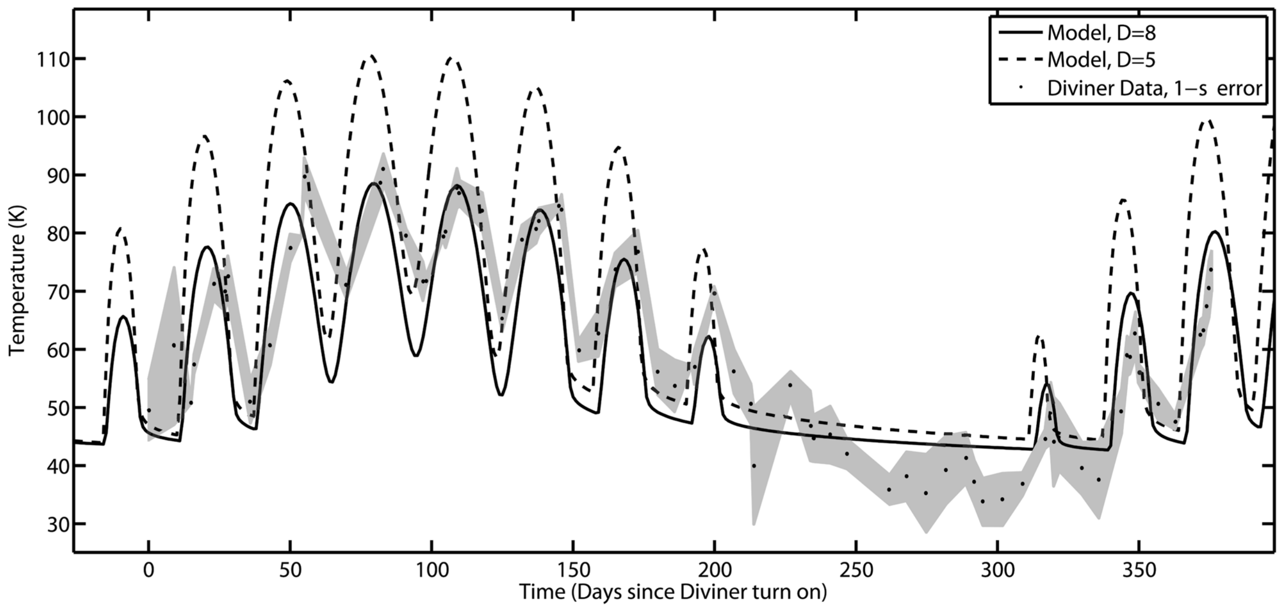

Figure 11. Modeled current temperatures at the center of Shackleton crater as compared to brightness temperature measurements (which assume unit emissivity) for a 500 m box at the center of Shackleton from the Diviner Lunar Radiometer 100–400 micron channel. The D = 5 model uses observed crater geometry and albedo [*Haruyama et al.*, 2008]. D = 8 was found to be a better fit to Diviner data, likely owing to the conical nature of Shackleton. Model D = 8 is used throughout this paper. Slight changes in latitude, longitude, surface visible and thermal properties, crater orientation, surface roughness, diameter to depth ratio, and a nonpoint-like Sun can all be adjusted as data warrants.

grains, equation (15)), where parameters k_c varies with density at depth z (as in equation (16)):

$$\rho = 1000 * \left[1.9 - 0.65 e^{\left(\frac{z_e - z}{z_e}\right)}\right] \quad (14)$$

$$k = k_c \left(1 + \chi \left(\frac{T}{350}\right)^3\right) \quad (15)$$

$$k_c = k_d - (k_d - k_s) \frac{(1.9 - \rho/1000)}{0.65} \quad (16)$$

The best fit Apollo values were found to be k_s = 6E-4, k_d = 8.25E-3, and χ = 2.7 [*Langseth et al.*, 1976; *Keihm*, 1984]. Heat capacity was assumed temperature-dependent, as measured from Apollo samples [*Robie et al.*, 1970]. A detailed description of this model can also be found in the appendix of *Keihm* [1984] and returns essentially identical results to *Vasavada et al.* [1999] for their assumed density profile (which is similar to that of the Apollo 17 heat flow site).

[49] The bottom boundary condition to this model has a constant flux of 15 mW m^{-2}. This was nominally chosen as the approximate value measured at the Apollo 17 landing site [*Langseth et al.*, 1976; *Keihm*, 1984], which was believed to be less effected by heat flow anomalies. *Weiczorek and Philips* [2000] estimated global variation of this value from 11 to 34 mW m^{-2} due to local thorium concentrations. Buried topography can also have an equally large effect on heat flow [*Warren and Rasmussen*, 1987]. A sudden change in surface temperature boundary conditions (by roughly 200 K) will result in a change in near-surface heat flow by as much as a factor of two (causing the lines in Figure 12 not to be parallel), but the orbital transitions here are slow enough that systems can be assumed in equilibrium.

[50] In addition to Apollo data, recent surface brightness temperature data from the Diviner Lunar Radiometer, aboard the Lunar Reconnaissance Orbiter, provides verification for the accuracy of model predictions. Diviner is a nine channel visible and infrared radiometer measuring the lunar surface at 0.3 to 400 microns [*Paige et al.*, 2009]. Figure 11 illustrates modeled surface temperatures within Shackleton compared to derived brightness temperature from Diviner longest wavelength (100–400 micron), and therefore most sensitive to low temperature, channel.

[51] Variations in albedo and emissivity have little net effect on temperatures, while a change in the diameter to depth ratio, D, can cause a large effect (as seen in Figure 11). The temperature of the floor of a shaded crater is determined primarily by the angle at which the floor views the warm, Sunlit portion of the crater wall. Craters with greater diameter to depth ratios are shallower, meaning that the floors see the walls at larger angles and therefore remain cooler [*Paige et al.*, 1992; *Vasavada et al.*, 1999]. Though Shackleton is flat floored with conical walls and relatively deep for a crater its size (D = 5) [*Haruyama et al.*, 2008], we model it as a shallow bowl-shaped crater (D = 8). This assumption better approximates the true scattering geom-

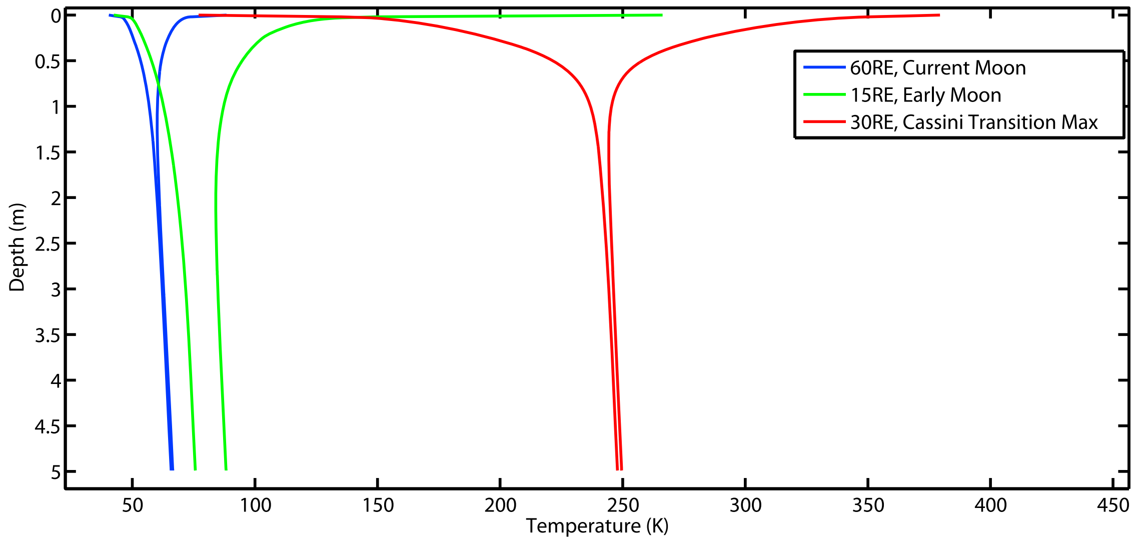

Figure 12. Maximum and minimum subsurface temperature variations over a precession cycle at 15 RE, 30 RE, and 60 RE.

etry within Shackleton while still allowing us to use the analytical solution for bowl-shaped craters. This change is highly consistent with both Diviner data and the Selene modeled 88 K summer solstice temperature [*Haruyama et al.*, 2008].

[52] The model here includes a 1.5 degree tilt (to 50° east of north) of Shackleton's rim as observed by the Selene mission [*Haruyama et al.*, 2008]. The tilt modulates the ratio between maximum and minimum monthly temperatures in a crater. The model was run for three precession periods with a time resolution of ~100–300 s (depending on temperatures). Results were extrapolated only from the third precession cycle to allow for thermal equilibrium of deep layers.

4.2. Surface and Subsurface Temperature History

[53] The general agreement with Apollo subsurface, as well as Diviner and Selene surface measurements validate this model for use in estimating past near-surface temperatures.

[54] In examining this past thermal history we again break the lunar history into three periods (with very rough time estimates): (1) an early period of large inclination driven

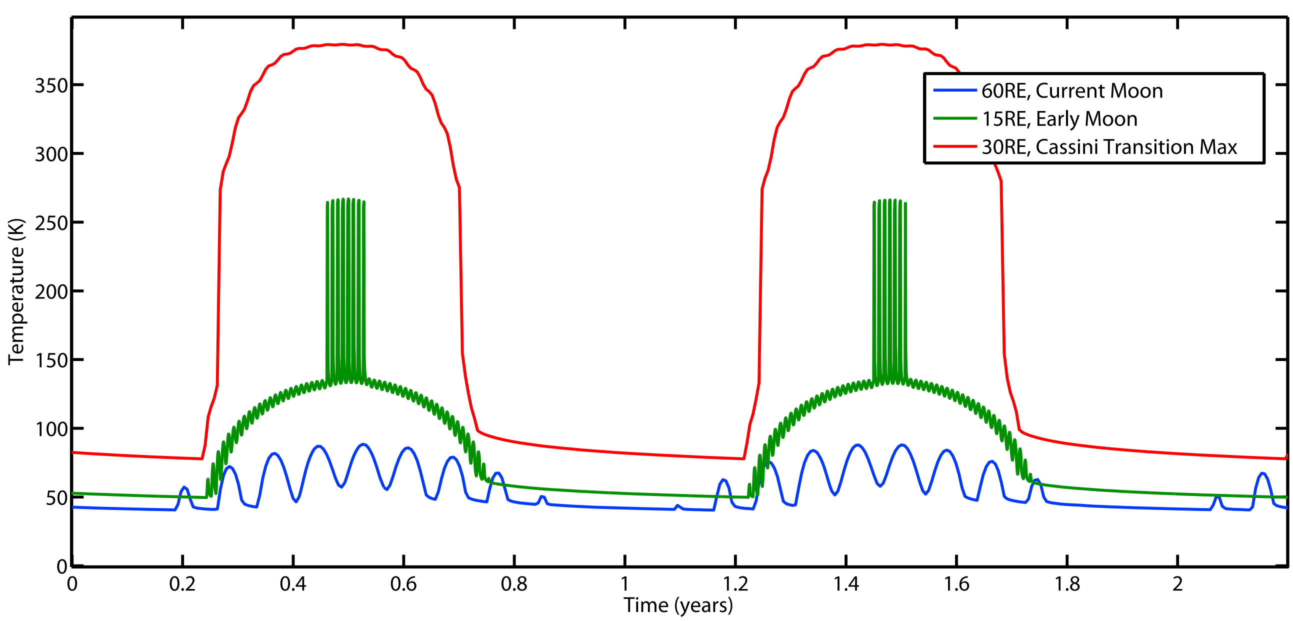

Figure 13. Yearly surface temperatures of Shackleton crater floor at 60 RE, 15 RE, and 30 RE (the current temperatures, early lunar epoch, and peak of the Cassini transition). Note the diurnal period was only about 3.4 days long at 15 RE, and the Sun only occasionally peaks over the horizon during this part of the precession cycle (the 15 RE line represents the first 2 years in Figure 9a).

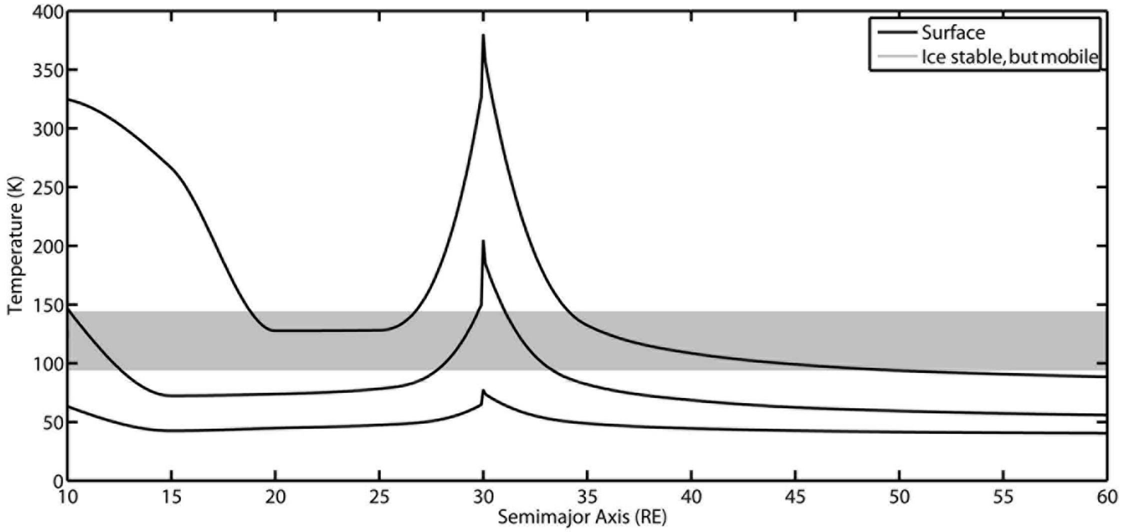

Figure 14. Maximum, minimum, and mean surface temperatures for modeled history of Shackleton crater. The shaded region approximates the temperature range under which ice will be stable at the surface but mobile enough to be buried by thermal diffusion.

variations (when the Moon was at 15 RE semimajor axis, >3.5 Gya), (2) a middle period of high obliquity surrounding the Cassini state transition (at 30 RE semimajor axis, >2.5, <4.0 Gya), and (3) the current low-obliquity era (at 60 RE semimajor axis, <2.5 Gya). Figures 11–15 present model results for the floor of Shackleton crater during each of these epochs.

4.3. Early History

[55] During the early lunar history (15 RE semimajor axis) large inclination variations modulated the amount of reflected light incident on the crater floor and θ_{max} varied greatly (from 1 to 14° over each precession cycle). At this semimajor axis, Shackleton surface temperatures reached a precessional period maximum of about 266.3 K and minimum of 42.4 K with a mean surface temperature of 72.2 K. The 266.3 K maximum temperatures occur only during the height of the precession cycle, when the crater floor receives a few diurnal cycles of direct illumination. In years not receiving direct illumination, maximum temperatures range between 82 K and 135 K. The large precessional period variations (54.8 years) reached deeper

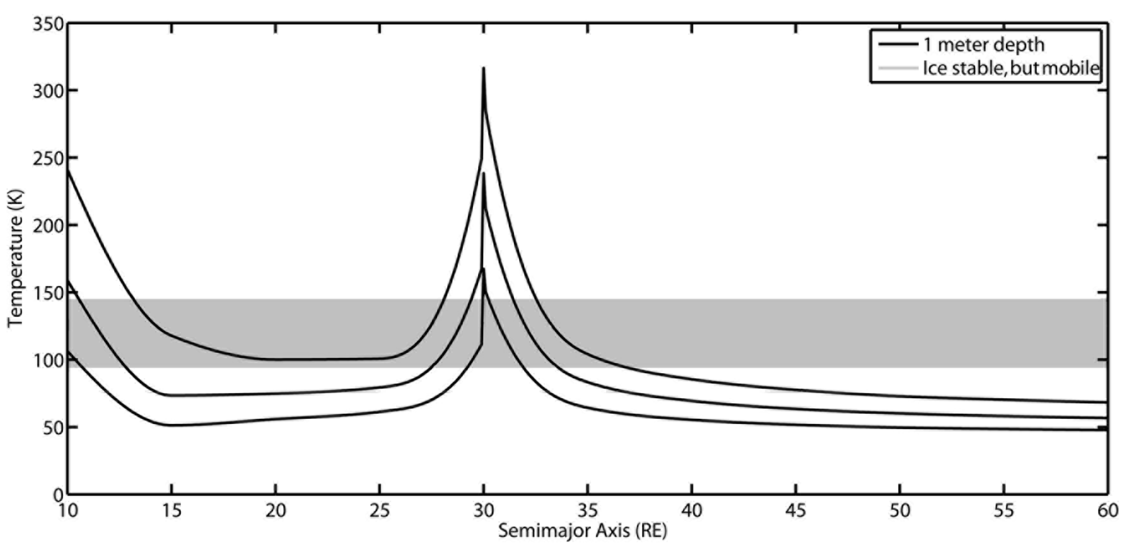

Figure 15. Maximum, minimum, and mean temperatures at 1 m depth for modeled history of Shackleton crater. The shaded region approximates the temperature range under which ice will be stable at the surface but mobile enough to be buried by thermal diffusion. Note that the temperature-dependent conductivity heats the subsurface to ~250 K during the Cassini state transition while surface temperatures only reach ~204 K (Figure 14).

than diurnal or yearly cycles causing relatively substantial 12.5 K (~75.7 to 88.2 K) variations in temperatures at 5 m depth. Geothermal heat causes a steady rise of roughly 2 K per meter down to depth. The geothermal gradient becomes linear as model thermal conductivities become nearly constant after about 2 m depth and radiogenic sources are assumed deeper than 10 m (Figure 12).

4.4. Cassini Transition

[56] As inclination variations decreased and the obliquity grew, craters like Shackleton ceased to be permanently shadowed. Temperatures reached their maximum during the peak of the Cassini state transition when $\theta_{\max}$ varied between 71.1 and 82.9° (blue circles, Figure 7). Yearly surface temperatures neared a maximum of 379.4 K during the 6 month long summer then plunged to 77.1 K during the long winter. Annual surface mean temperatures were about 204.2 K, (coincidentally nearly identical to those measured at the Apollo 15 landing site) [*Langseth et al.*, 1976]. Like at the Apollo sites, the temperature dependence of the lunar soil caused the subsurface mean to grow substantially with depth, calculated here to be nearly 249.0 K at 5 m depth (Figure 12).

[57] Declining precession-scale inclination variations caused only a ±1.7 K variation in temperatures at 5 m depth. As discussed in section 5, it is difficult to imagine ice surviving long under these conditions. Dissipation within the Moon would have driven the spin axis into a new stable configuration relatively quickly, causing these seasons of extreme temperatures to be short lived (likely ~10^5 years) [*Ward*, 1975].

[58] Though these maximum temperatures did not last long, temperatures after the Cassini transition were not dramatically cooler. Entering Cassini state 2, $\theta_{\max}$ varied between roughly 43.1° and 54.9°. This brought Shackleton floor temperatures up to 356.4 K during the summer and down to 73.6 K during the long polar night. Year surface mean temperatures hovered around 184.9 K (illustrated in Figures 14 and 15). As the duration of these illumination conditions depended not on dissipation within the Moon, but rather tidal dissipation within the Earth, similar temperatures likely persisted for millions of years as obliquity slowly decreased with the growing semimajor axis.

4.5. Present Era

[59] As inclination variations nearly ceased and obliquity decreased, the current lunar permanently shadowed regions would begin to appear. Shackleton crater would become shadowed at a $\theta_{\max}$ below 14.04° (see section 3.2). Therefore, permanently shadowed regions, like Shackleton, likely did not exist prior to Moon reaching ~31 RE semimajor axis. Currently, with a modeled yearly surface minimum of 40.4 K, mean of 55.9 K, and 88.4 K maximum make it a good candidate for surface ice capture. However, as discussed in section 5, the slow thermal mobility of ice at temperatures below roughly 96 K might prevent this ice from migrating very deeply into the subsurface via thermal diffusion processes [*Schorghofer and Taylor*, 2007]. The subsurface sees only a slight rise to a mean of 66.1 K at 5 m depth. A summary of this thermal evolution is shown in Figures 12–15.

5. Discussions on Thermal Stability and Mobility of Volatiles

[60] In this section we will summarize volatile stability and mobility by introducing a distinction between (1) permanent shadow: areas that do not receive direct sunlight, (2) cold traps: areas where water ice is over geologic time, (3) subsurface cold traps: areas where regolith cover allows a cold trap to exist only in the subsurface, and (4) ice traps: areas that can potentially collect ice and thermally drive it into the shallow subsurface. These terms tend to be used interchangeably, but are deserving of distinct redefinition. As this paper does not attempt to provide a detailed model of past supply and loss processes, these definitions highlight only the potential to trap or retain ice as controlled by temperature.

5.1. Permanent Shadow

[61] Many areas on the Moon currently lie in permanent, or more correctly persistent, shadow. However, this distinction alone does not imply that they will be good places to collect water ice. As mentioned in section 4.4, the floor of Shackleton is shadowed when the Sun is less than 14.04° above the horizon. In addition, when reflected visible and reradiated infrared light are accounted for, shadowed regions can still be relatively warm [*Ingersoll et al.*, 1992; *Vasavada et al.*, 1999]. Though Shackleton is modeled to have become shadowed around 31 RE semimajor axis, mean annual temperatures were still above 130 K and too warm to be labeled as a classic “cold trap.”

5.2. Cold Traps

[62] The definition of a cold trap has traditionally been an area in which one kg m^{-2} of water would survive on the lunar surface for one billion years [*Watson et al.*, 1961a; *Vasavada et al.*, 1999; *Schorghofer and Taylor*, 2007]. There is nothing unique about this loss rate, but it serves as a useful benchmark for ice stability over geologic time. When only thermal loss processes are accounted for, a loss rate of one kg m^{-2} Gyr^{-1} to occur at 101.35 K.

[63] This loss rate can be calculated

$$E = \frac{P_{sv}}{\sqrt{2\pi RT/\mu}} \tag{17}$$

where E is the sublimation rate (kg m^{-2} s^{-1}) [*Langmuir*, 1913; *Watson et al.*, 1961b], R the Boltzmann constant (8.314 J K^{-1} mol^{-1}), T temperature, and μ the molecular weight of water. This formulation represents the maximum possible sublimation rate as it assumes a condensation coefficient of unity (actual values may fall between 0.7 and 1) [*Schorghofer and Taylor*, 2007]. P_{sv}, the saturation vapor pressure, can be calculated

$$P_{sv} = P_t \exp\left[\frac{-Q}{R}\left(\frac{1}{T} - \frac{1}{T_t}\right)\right] \tag{18}$$

where P_t (for H_2O, 611.7 Pa) and T_t (237.16 K) are the triple point pressure and temperature, and Q is the latent heat of

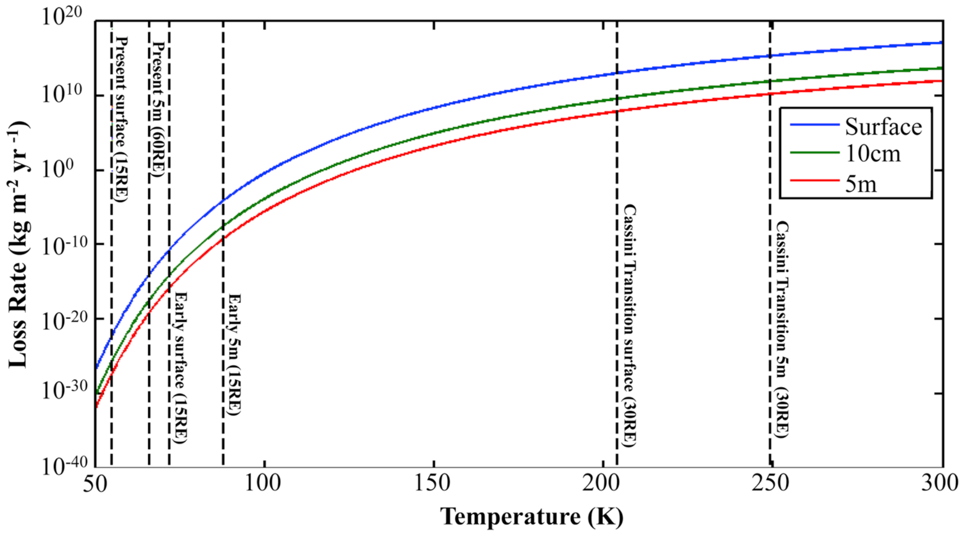

Figure 16. Rate of ice loss (kg m^{-2} Gyr^{-1}) for ice under vacuum at the surface and buried by a 10 cm or 5 m layer of 75 μm grain size particles (as in the work of *Schorghofer and Taylor* [2007]). The vertical lines mark the calculated mean surface and subsurface temperatures at 15 RE, 30 RE, and 60 RE semimajor axis.

sublimation (Q/R ≈ 6130 K). These derivations can be used for any volatile with by changing P_t, T_t, Q, and μ. If buried, either by thermal migration or gardening, beneath a diffusion layer (z m thick) of particles diameter δ (75 μm here), sublimation rate, J (kg m^{-2} s^{-1}, which is roughly equal to mm s^{-1}) is estimated by *Schorghofer and Taylor* [2007] as

$$J = \frac{\mu \delta E}{2z} \qquad (19)$$

which assumes diffusion to be well within the Knudsen regime (in which diffusion is controlled by collisions with pore walls rather than other molecules), and is illustrated in Figures 16 and 17 and Table 1.

[64] This also implies a distinction between surface and subsurface cold traps. Comparison of equations (17) and (19) show that the introduction of even a thin diffusive barrier can cause ice to be stable in the near subsurface in areas where it is not stable at the surface (Figure 16). In addition, the extreme thermal insulation provided by the low thermal conductivity of the lunar regolith also serves to protect even the shallow subsurface from experiencing large diurnal temperature swings. Ice can then be stable at depth until downward motion is inhibited by geothermal heat.

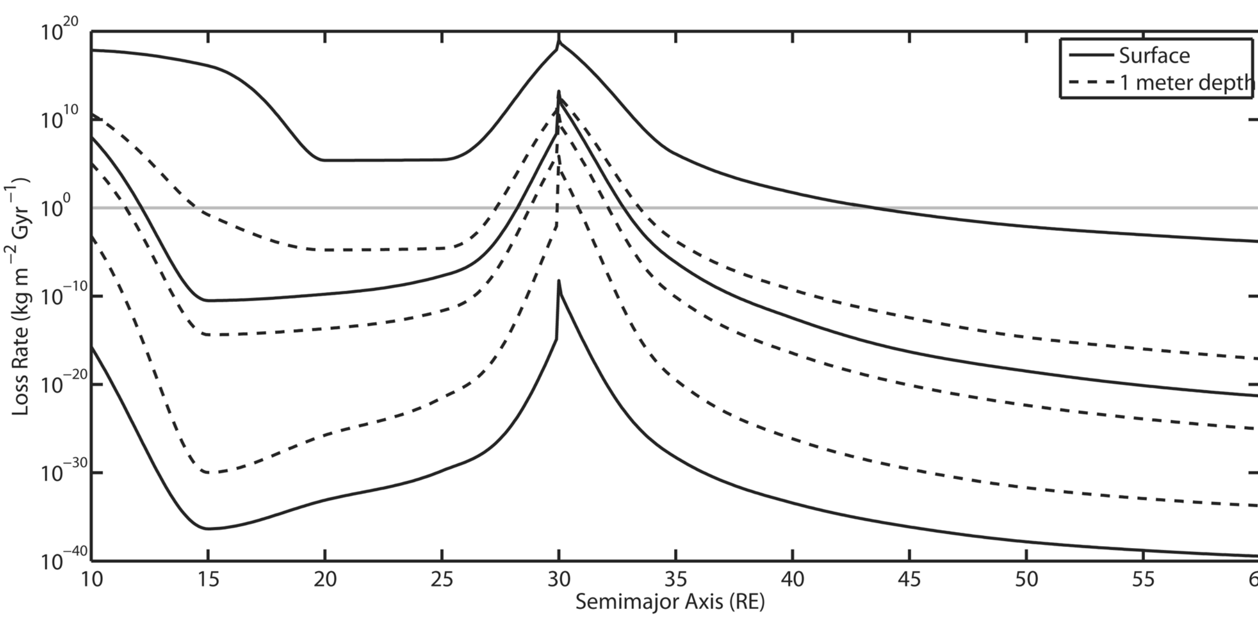

Figure 17. Instantaneous rate of ice loss (kg m^{-2} Gyr^{-1}) for maximum, minimum and mean temperatures in Shackleton crater as a function of semimajor axis (assuming 75 μm grain diffusion barrier for 1 m depth calculation). The horizontal gray line marks the “cold trap” loss rate of 1 kg m^{-2} Gyr^{-1}.

Table 1. Sublimation Rate of a Layer of Ice Assuming the Mean and Maximum Temperature at the Lunar Surface, at 10 cm, and at 5 m Depth and 75 μm Grain Lag

	15 RE Max	15 RE Mean	30 RE Max	30 RE Mean	60 RE Max	30 RE Mean	101.35 K
Surface							
T (K)	266	72	379	204	88	55	101.35
J (kg m^{-2} Gyr^{-1})	1.2E16	2.2E-11	9.8E18	1.2e13	1.1E-4	9.1E-23	1.0E0
10 cm							
T (K)	118	73	317	238	68	56	101.35
J (kg m^{-2} Gyr^{-1})	1.8E0	2.7E-14	1.7E14	3.1e11	5.7E-17	2.5E-25	3.8E-4
5 m							
T (K)	88	82	250	249	66	66	101.35
J (kg m^{-2} Gyr^{-1})	8.2E-10	5.1E-12	2.1E10	1.9e10	7.5E-20	7.5E-20	7.5E-6

A model describing surface and subsurface cold traps would define the maximum volume available for ice and would be much larger than current cold trap estimates [*Paige et al.*, 2010]. This volume would grow with increased regolith thermal conductivity and therefore with ice content itself.

5.3. Ice Traps

[65] Cold traps are however in no sense necessarily full or likely to contain any ice unless supply and thermal conditions allow. This leads us to define ice traps, which are neither a subset of permanent shadow or cold traps. Ice traps are areas where thermal diffusion will be the dominant path of ice mobility. In an ice trap, temperatures are cold enough that ice may collect at the surface for part of an orbital cycle, but warm enough that diffusive transport along thermal gradients would be able to drive ice downward. Ice traps are not always permanently shadowed regions, as they may receive a few days of direct sunlight a year (as in the example at 15 RE). As seen below, their temperatures likely exceed 100 K so they also do not fit the traditional definition of cold traps.

[66] An ice trap is inherently defined by supply and loss; the greater the surface supply rate and slower the (non-thermal) loss processes, the higher the temperature at which ice can survive there. The Moon has a complex history of supply and loss which, through effect of ice on regolith thermal properties, has an equally complicated effect on surface and subsurface temperatures. Rather than approaching a supply-dependent model, here we seek a range of temperature conditions within which supplied ice might be retained in the subsurface by diffusion. *Schorghofer and Taylor* [2007] examine two models of ice deposition, a slow, continuous supply and a temporary ice cover at a constant temperature. Both result in similar, small quantities of subsurface ice, but the ice cover would result in a large effect on surface thermal properties, altering our modeled temperatures. Following the slow supply model, with residence time of a molecule defined as $\tau = E/\Theta$ (where Θ is the number of molecules in a monolayer), they describe an equilibrium surface density formed from a steady supply by

$$\sigma(\infty) = \frac{s}{\frac{1}{2\tau} + \frac{\nu}{\Theta}} \tag{20}$$

where s is the supply rate and υ is the nonthermal loss rate (both in molecules Gyr^{-1}). An error function solution for diffusion of ice into the subsurface was found to result in a column integrated ice mass (kg m^{-2}), m:

$$m = \sigma(\infty)\sqrt{\frac{2t}{\pi\tau}} \tag{21}$$

Assuming their chosen rates of supply, $s\mu$ = 100 kg m^{-2} Gyr^{-1}, and weathering loss rate, $\upsilon\mu$ = 1000 kg m^{-2} Gyr^{-1}, (where μ is the mass of an H_2O molecule) and a time period, t, of a billion years, equation (21) peaks in deposition of ice to the subsurface at a steady state temperature around 117 K. Above this temperature, supplied ice sublimates rapidly, leaving the subsurface *supply limited*. Below this temperature, they find ice migration slows dramatically, causing ice retention to be *diffusion limited*. Given their unspecified background loss process (Lyman Alpha, cosmic rays, etc), the 117 K maximum value (of m~10^{-3} kg m^{-2} for their standard supply) drops by 2 orders of magnitude for temperatures higher than ~145 K and lower than ~96 K. In their formulation of a constant supply, the maximum value of subsurface ice, m, scales directly with supply rate (roughly as supply [units kg m^{-2} Gyr^{-1}] × 10^{-5} Gyr). However, due mainly to the assumption of constant temperatures with depth, this model results in exceedingly small amounts of ice.

[67] Although the work of *Schorghofer and Taylor* [2007] assumes a constant temperature with time, which is not necessarily applicable for the time varying temperatures described in this paper, it can serve as a guideline for expected ice stability. As has been demonstrated in models of Martian ice deposition [*Mellon and Jakosky*, 1993; *Schorghofer and Aharonson*, 2005; *Schorghofer*, 2010], time varying surface temperatures can allow large amounts of ice to be collected. Ice is driven downward along thermal gradients into the subsurface during warmer parts of the year and relatively immobile during colder parts of the year. In the top few centimeters for or dry regolith of Shackleton, thermal gradients can be very large, on the order of 10^3 K m^{-1}, and can cause large vapor pressure gradients (by equation (18)) if there is a large enough supply to saturate, which happens below ~153 K for the supply described in equation (20)). Even if different physics are driving ice mobility, a few important rules of thumb should hold from the constant temperature case: in areas constantly below about 96 K, such as Shackleton crater is at present, molecular diffusion is too slow to build substantial amounts of ice in the subsurface and ice will remain on the surface, subject to a variety of loss processes that may destroy ice long before slow gardening

processes can bury it. Above about 145 K, even large surface supplies will result in very little ice retention.

[68] Simplifying the constants brought with a complete model of history of ice supply, loss, and unmeasured effects of ice on thermal and diffusive properties, we approximate an ice trap by the 96–145 K window, where, by the preceding arguments, water molecules can be considered stable and yet mobile in the near lunar subsurface. In this temperature range, if supplied to the surface in great enough quantities, water molecules will be driven along very large thermal gradients (again $\sim 10^3$ K m^{-1}) into the first few centimeters subsurface, where they would be protected from surface erosion [*Arnold*, 1979] and migrate slowly downward (on lesser gradients $\sim 10^2$ K m^{-1}). Constant temperature calculations show thermal burial at ice trap temperatures is faster than burial by impact gardening, but show only small amounts of ice growth [*Schorghofer and Taylor*, 2007; *Crider and Killen*, 2005]. The assumption that time varying temperatures in this range will form more ice under lunar conditions requires further study, but the rates of subsurface migration at a given temperature should exceed those in the constant temperature model [*Schorghofer and Aharonson*, 2005]. So, while gardening processes may drive ice deeper over millions of years (given the right supply, temperature range, and gradients) thermally driven diffusion should provide rapid burial below the important top few centimeters. At temperatures much above 160 K, only adsorbed water would survive [*Dyar et al.*, 2010]. Much below 96 K, the only downward movement is provided by the relatively slow processes of impact gardening and burial [*Crider and Vondrak*, 2003a, 2003b; *Crider and Killen*, 2005].

[69] Figures 14 and 15 illustrate that Shackleton crater experienced ice trap conditions only before about 26 RE and between roughly 32 to 45 RE (as gauged by mean and maximum temperature excursions). These periods marks the time window in which Shackleton crater would have been most thermally suited to collect ice if it were supplied, but does not imply that a substantial amount of ice was actually delivered to Shackleton during that period. Each crater or shadowed region will have its own insulation history as dictated by its latitude and local topography. Lack or presence of ice in a particular crater therefore may be diagnostic of the history of volatile supply to the Moon. If an ice trap crater evolves into a cold trap, this relic period may be frozen in, preserving ice that might otherwise been unstable. Shackleton is a polar crater, though its history can guide the understanding of processes in the greater polar region. Future modeling work by the authors will aim to examine depositional processes for the entire lunar polar regions in more detail.

6. Conclusions

6.1. Early History

[70] Assuming an impact formed Moon which had cooled substantially by the time it had reached 15 RE, the early lunar poles likely presented a relatively ideal environment for capturing and retaining water ice. Surface temperatures were generally near the 96–145 K ice trap temperature at which ice capture and shallow burial will be most efficient (Figures 12–14) [*Schorghofer and Taylor*, 2007]. Deeper areas remained cold enough to act as a subsurface cold trap (Figure 14). Brief periods of direct insolation might erode some surface ice, but would provide pulses of heat that might drive shallowly buried ice even deeper. Due to the large precession cycle oscillations of the lunar orbit, thermal waves had relatively large amplitudes at depth and could have driven supplied ice to a few meters depth.

[71] Combined with possible abundant Late Heavy Bombardment ice delivery, a crater like Shackleton might have captured surface ice during cold periods of the precession cycle and, if surface supplies were large enough to counteract losses, driven it to depth during warmer parts of the cycle. As ice increases the thermal conductivity of the subsurface, the thermal waves at every time scale to reach much deeper than described in section 4.2. With dry regolith, the lowest maximum temperature occurs at about 2.5 m, meaning ice should be most stable at this depth. Since icy regolith will have higher conductivity, surface thermal variations can travel deeper, possibly tens of meters into the subsurface. The presence of ice therefore would drive ice further into the subsurface, until inhibited by the geothermal gradient.

6.2. Cassini Transition

[72] It is unlikely, but not impossible, that Shackleton crater could have retained ice in the subsurface through the transition. With subsurface average temperatures of 249.0 K at 5 m, even deep ice would be mobilized within a few years. The lowest maximum temperature 244 K at 1.48 m depth is still much too high to harbor interstitial pore ice.

[73] However, before reaching this equilibrium temperature state, ice will not necessarily travel upward. If pore space is available, the slow surface thermal wave may have driven ice downward into regolith still cold from the past shadowed periods (as the green curve in Figure 12 evolves to the red curve). This downward mobility would be inhibited, but not necessarily prevented, as regolith density increases with depth.

[74] The floor of our modeled cater (and effectively all of the lunar polar region) received roughly half a year of direct illumination for the entire time the Moon lay between 27 and 31 Earth radii away from its parent. Though the lunar recession rate is unknown, this likely represents a period of at least 10^8 years [*Bills and Ray*, 1999]. Even assuming low-conductivity lunar regolith (thermal diffusivity $1e^{-6}$ to $1e^{-7}$ m^2 s^{-1}), a surface thermal wave would reach ~10 km within 10^8 years (with an amplitude e^{-1} times that of the surface wave). Combined with the effects of geothermal heating, it is likely that all subsurface cold traps were rendered devoid of pore ice.

[75] Processes such as sublimation cooling, especially low-density regolith (with low solid thermal conductivity), or compacted regolith (with low temperature-dependent conductivity and porosity) would slow this diffusion rate down, but not dramatically. More likely, surface adsorbed or chemically bonded water could be retained at these high temperatures. Monolayers of water or OH chemiosorbed to grain surfaces might be stable to 300–500 K [*Dyar et al.*, 2010], but these quantities would be much less than could be preserved in pore spaces and less then amounts observed by the LCROSS mission [*Colaprete et al.*, 2010], implying

that ice is of more recent origin. If the cold traps were truly ice rich prior to the Cassini transition, it is possible that plentiful strong bonds might be able to form on grain surfaces and defects. In addition, if transient water formed during this hot period it may have had a chance to chemically alter regolith grains. Assuming an 1 K m^{-1} linear increase in temperature with depth due to geothermal heat, temperatures of 273 K become possible about 30 m below the surface. It is unclear whether water molecules at this depth would volatilize or percolate downward along cracks and available pore space.

6.3. Current Era

[76] Posttransition, the subsurface, warm from geothermal heat (and the heat of the Cassini transition) but not reached by the short-period yearly thermal waves (reaching down to roughly 1.4 m), will tend to be warmer than the surface. Due to this thermal gradient, ice accumulating at the surface of a post-Cassini lunar cold trap will be most stable at or very near the surface. In the unlikely scenario any early lunar ice was driven downward by the Cassini transition and survived, it might still be slowly rising to fill the lunar cold traps from below. Such ice would have had to have been buried very deep and due to cold temperatures this upward migration would be slow, so it would likely be disconnected from the present surface. Shortly after the Cassini transition, warm temperatures mean any surviving subsurface ice might have been more mobile (as the red curve in Figure 12 evolves to the blue curve).

[77] This possible subsurface ice would evolve toward the point of lowest maximum temperature, slowing as temperatures cooled. In the current lunar environment, ice would be thermally driven to the point with the lowest maximum temperature, about 1.5 m depth in our model of Shackleton crater. Even accounting for impact gardening [*Crider and Vondrak*, 2003a, 2003b], ice found much below this depth may require an ancient origin. If diffusing up from below, ancient, pre-Cassini transition, ice should increase in concentration with depth; surface derived ice would do the opposite.

[78] Surface ice can be thought of as thermally immobile once a crater's average temperature falls below about 96 K (~45 RE for maximum temperatures in our model). After reaching such temperatures, only burial from nearby impact ejecta or by impact gardening can provide downward motion of surface ice [*Crider and Vondrak*, 2003a, 2003b; *Vondrak and Crider*, 2003; *Arnold*, 1975; *Gault et al.*, 1974]. In the modern lunar environment, only slightly warmer areas around the edges of cold traps, where mean temperatures might hover about 96–145 K, will be able to both retain and bury ice by vapor diffusion [*Schorghofer and Taylor*, 2007] ("lunar permafrost" in the work of *Paige et al.* [2010]).

[79] In addition, once posttransition cold traps reappear, other compounds less volatile than water will also compete for pore space [*Zhang and Paige*, 2009; *Watson et al.*, 1961a, 1961b]. These volatiles may fill up many voids and adsorbtion sites at higher obliquities before water is stable. As seen in the LCROSS impact, a wide variety of volatiles, not just water, likely fill the lunar cold traps [*Colaprete et al.*, 2010].

6.4. Summary and Discussion

[80] Figures 16 and 17 and Table 1 summarize the huge range of relative stability of water ice in the near subsurface over the lunar history. Both the early and present lunar polar thermal environments provided regions capable of storing water ice. However, it is doubtful that interstitial pore ice could have survived even at depth with the inferred loss rates associated with the Cassini state transition. This leaves a period, when the Moon resided between ~32 to 45 RE, during which Shackleton might have been a good ice trap, able to thermally capture and thermally bury supplied water. After that point, ice can be considered thermally immobile, and while the crater floor might capture more surface ice, it will remain on the surface, subject to surface erosion processes, unless buried by impacts. The authors are continuing further work to quantitatively verify these assertions with a full vapor diffusion model. As Shackleton crater is not representative of the evolution of other polar environments, new topographic data is being used to quantify the geographical and temporal extent of regions where thermal burial would dominate.

[81] Mercury also has a small obliquity (1.0 to 2.3 arcmin) [*Yseboodt and Margot*, 2006], so that areas inside craters near its poles remain in permanent shadow. Radar bright deposits are seen there, and have been shown to coincide with shadowed areas cold enough to ensure long-term ice stability, suggesting that the radar signature comes from massive deposits of water ice [*Slade et al.*, 1992; *Paige et al.*, 1992; *Vasavada et al.*, 1999; *Harmon and Slade*, 1992; *Harmon et al.*, 1994, 2001].

[82] Despite some tantalizing evidence, radar and neutron spectrometer data have given little direct evidence for lunar near-surface ice in quantities comparable to that believed to exist on Mercury [*Nozette et al.*, 1996; *Simpson and Tyler*, 1999; *Stacy et al.*, 1997; *Margot et al.*, 1999; *Feldman et al.*, 2001; *Campbell et al.*, 2006; *Spudis et al.*, 2010]. The recent detections of widespread surface water and OH by the Chandrayaan, Cassini, and Deep Impact missions [*Pieters et al.*, 2009; *Clark*, 2009; *Sunshine et al.*, 2009], and of cold-trapped polar ice by LCROSS and LRO missions [*Colaprete et al.*, 2010], have shown that near-surface lunar ice reservoirs do exist, but not in the concentrations that seem to be present on Mercury. In short, though their current polar environments are similar, Mercury and the Moon appear to have very different volatile inventories.

[83] A partial explanation for this difference may lie in the difference in loss processes driven by the orbital and rotational histories of these two bodies. The present obliquity of Mercury is small [*Yseboodt and Margot*, 2006; *Bills and Comstock*, 2005] and may have been so for much of its history. In contrast, the Moon has experienced relatively recent periods during which presently shadowed polar craters would have been fully illuminated [*Ward*, 1975; *Arnold*, 1979]. It is interesting to note that under its current orbital most of Mercury's polar craters are warmer than those on the Moon and many experience ice trap temperatures [*Vasavada et al.*, 1999]. In thermal terms, many present-day polar environments on Mercury could be a good analog for those on the Moon at ~35 RE. Mercury's orbital history has not been well constrained, but the planet is not believed to have undergone a large Cassini transition like the Moon, and

therefore may have had a comparably long time at its current orbital conditions and long time to collect near-surface ice.

[84] Returning to the Moon, if signs of pre-Cassini transition ice (deep ice or more likely the chemical alterations caused by the past presence of this ice) were detectable, it should only be present in the oldest craters. It might therefore be possible to date the time of the Cassini transition by dating youngest of these craters, serving as a constraint on the rate of recession of the lunar semimajor axis. Presence or absence of certain volatiles, adsorbed molecules, or chemically altered regolith might also help constrain maximum lunar temperatures and therefore maximum orbit parameters. In addition, if a dramatic impact induced reorientation of the lunar surface has occurred since the time of ice deposition [*Ong and Melosh*, 2010], chemically anomalous *paleoice traps* might even exist.

[85] As each current cold trap had a period where it was most efficient at thermal ice burial, the location of current ground ice on the Moon might also constrain the obliquity and time at which it was deposited. The presence of ice in a specific crater may imply either an increase in water flux or large comet impact during that period. As data from planetary subsurfaces increase, further modeling of stability and movement of subsurface volatile deposits should be a promising avenue with which to explore the orbital and climate histories of wide range of solar system bodies.

[86] **Acknowledgments.** The authors would like to thank Norbert Schorghofer, Jean-Pierre Williams, Ashwin Vasavada, Paul Hayne, Jean-Luc Margot, Ben Greenhagen, and Hermann Engelhardt for their useful reviews and discussion as well as Jack Wisdom for his aid in reconstructing the work of *Touma and Wisdom* [1994].

References

Arnold, J. R. (1975), A Monte Carlo model for the gardening of the lunar regolith, *Earth Moon Planets*, *13*, 159–172, doi:10.1007/BF00567513.
Arnold, J. R. (1979), Ice in the lunar polar regions, *J. Geophys. Res.*, *84*, 5659–5668, doi:10.1029/JB084iB10p05659.
Atobe, K., and S. Ida (2007), Obliquity evolution of extrasolar terrestrial planets, *Icarus*, *188*, 1–17, doi:10.1016/j.icarus.2006.11.022.
Bills, B. G. (2005), Free and forced obliquities of the Galilean satellites of Jupiter, *Icarus*, *175*, 233–247, doi:10.1016/j.icarus.2004.10.028.
Bills, B. G., and R. L. Comstock (2005), Forced obliquity variations of Mercury, *J. Geophys. Res.*, *110*, E04006, doi:10.1029/2003JE002116.
Bills, B. G., and R. D. Ray (1999), Lunar orbital evolution: A synthesis of recent results, *Geophys. Res. Lett.*, *26*(19), 3045–3048, doi:10.1029/1999GL008348.
Bills, B. G, W. B. Moore, M. A. Siegler, and D. A. Paige (2010), Obliquity during a Cassini-state transition, *Lunar Planet. Sci.*, *XLI*, Abstract 1752.
Buhl, D., W. J. Welch, and D. G. Rea (1968), Reradiation and thermal emission from illuminated craters on the lunar surface, *J. Geophys. Res.*, *73*, 5281–5295, doi:10.1029/JB073i016p05281.
Campbell, D. B., B. A. Campbell, L. M. Carter, J. Margot, and N. J. Stacy (2006), No evidence for thick deposits of ice at the lunar south pole, *Nature*, *443*, 835–837, doi:10.1038/nature05167.
Clark, R. N. (2009), Detection of adsorbed water and hydroxyl on the Moon, *Science*, *326*, 562–564, doi:10.1126/science.1178105.
Colaprete, A., et al. (2010), The detection of water within the LCROSS ejecta plume, *Science*, *330*, 463–468, doi:10.1126/science.1186986.
Colombo, G. (1966) Cassini's second and third laws, *Astron. J.*, *71*, 891–896.
Crider, D. H., and R. Killen (2005), Burial rate of Mercury's polar volatile deposits, *Geophys. Res. Lett.*, *32*, L12201, doi:10.1029/2005GL022689.
Crider, D. H., and R. R. Vondrak (2003a), Space weathering effects on lunar cold trap deposits, *J. Geophys. Res.*, *108*(E7), 5079, doi:10.1029/2002JE002030.
Crider, D. H., and R. R. Vondrak (2003b), Space weathering of ice layers in lunar cold traps, *Adv. Space Res.*, *31*, 2293–2298.
Darwin, G. (1880), On the secular changes in the elements of the orbit of a satellite revolving about a tidally distorted planet, *Philos. Trans. R. Soc. London*, *171*, 713–891, doi:10.1098/rstl.1880.0020.
Dyar, M. D., C. C. Hibbitts, and T. M. Orlando (2010), Mechanisms for incorporation of hydrogen in and on terrestrial planetary surfaces, *Icarus*, *208*, 425–437, doi:10.1016/j.icarus.2010.02.014.
Feldman, W. C., et al. (2001), Evidence for water ice near the lunar poles, *J. Geophys. Res.*, *106*, 23,231–23,251, doi:10.1029/2000JE001444.
Garrick-Bethell, I., J. Wisdom, and M. T. Zuber (2006), Evidence for a past high-eccentricity lunar orbit, *Science*, *313*, 652–655, doi:10.1126/science.1128237.
Gault, D. E., F. Horz, D. E. Brownlee, and J. B. Hartung (1974), Mixing of the lunar regolith, *Proc. Lunar Sci. Conf.*, *5th*, 2365–2386.
Goldreich, P. (1966), History of the lunar orbit, *Rev. Geophys.*, *4*, 411–439, doi:10.1029/RG004i004p00411.
Harmon, J. K., and M. A. Slade (1992), Radar mapping of Mercury: Full-disk images and polar anomalies, *Science*, *258*, 640–643, doi:10.1126/science.258.5082.640.
Harmon, J. K., M. A. Slade, R. A. Velez, A. Crespo, M. J. Dryer, and J. M. Johnson (1994), Radar mapping of Mercury's polar anomalies, *Nature*, *369*, 213–215, doi:10.1038/369213a0.
Harmon, J. K., P. J. Perillat, and M. A. Slade (2001), High-resolution radar imaging of Mercury's north pole, *Icarus*, *149*, 1–15, doi:10.1006/icar.2000.6544.
Haruyama, J., et al. (2008), Lack of exposed ice inside lunar south pole Shackleton crater, *Science*, *322*, 938–939.
Hilton, J. L. (1991), The motion of Mars' pole. I. Rigid body precession and nutation, *Astron. J.*, *102*, 1510–1527.
Ingersoll, A. P., T. Svitek, and B. Murray (1992), Stability of polar frosts in spherical bowl-shaped craters on the Moon, Mercury, and Mars, *Icarus*, *100*, 40–47, doi:10.1016/0019-1035(92)90016-Z.
Keihm, S. J. (1984), Interpretation of the lunar microwave brightness temperature spectrum: Feasibility of orbital heat flow mapping, *Icarus*, *60*, 568–589, doi:10.1016/0019-1035(84)90165-9.
Kimball, H. H. (1925), Daylight illumination on a sloping surface: A correction, *Mon. Weather Rev.*, *53*(10), 448, doi:10.1175/1520-0493(1925)53<448:DIOASS>2.0.CO;2.
Kimball, H. H., and I. F. Hand (1922), Daylight illumination on horizontal, vertical, and sloping surfaces, *Mon. Weather Rev.*, *50*(12), 615–628, doi:10.1175/1520-0493(1922)50<615:DIOHVA>2.0.CO;2.
Kinoshita, H. (1977), Theory of rotation of the rigid Earth, *Celestial Mech.*, *15*, 277–326, doi:10.1007/BF01228425.
Langmuir, I. (1913), The vapor pressure of metallic tungsten, *Phys. Rev.*, *2*(5), 329–342, doi:10.1103/PhysRev.2.329.
Langseth, M. G., S. J. Keihm, and K. Peters (1976), Revised lunar heat-flow values, *Proc. Lunar Sci. Conf.*, *7th*, 3143–3171.
Leighton, R. B., and B. C. Murray (1966), Behavior of carbon dioxide and other volatiles on Mars, *Science*, *153*, 136–144, doi:10.1126/science.153.3732.136.
Margot, J., D. B. Campbell, R. F. Jurgens, and M. A. Slade (1999), Topography of the lunar poles from radar interferometry: A survey of cold trap locations, *Science*, *284*, 1658–1660, doi:10.1126/science.284.5420.1658.
Mellon, M. T., and B. M. Jakosky (1993), Geographic variations in the thermal and diffusive stability of ground ice on Mars, *J. Geophys. Res.*, *98*, 3345–3364, doi:10.1029/92JE02355.
Nozette, S., C. L. Lichtenberg, P. Spudis, R. Bonner, W. Ort, E. Malaret, M. Robinson, and E. M. Shoemaker (1996), The Clementine bistatic radar experiment, *Science*, *274*, 1495–1498, doi:10.1126/science.274.5292.1495.
Ong, L., and H. J. Melosh (2010), Reorientation of the Moon due to South Pole-Aitken basin ejecta, *Lunar Planet. Sci.*, *XLI*, Abstract 1363.
Paige, D. A., S. E. Wood, and A. R. Vasavada (1992), The thermal stability of water ice at the poles of Mercury, *Science*, *258*, 643–646, doi:10.1126/science.258.5082.643.
Paige, D. A., et al. (2009), The Lunar Reconnaissance Orbiter Diviner Lunar Radiometer Experiment, *Space Sci. Rev.*, *150*, 125–160, doi:10.1007/s11214-009-9529-2.
Paige, D. A., et al. (2010), Diviner observations of cold traps in the lunar south polar region: Spatial distribution and temperature, *Science*, *330*, 479–482, doi:10.1126/science.1187726.
Peale, S. J. (1969), Generalized Cassini's law, *Astron. J.*, *74*, 483–489, doi:10.1086/110825.
Peale, S. J., and P. Cassen (1978), Contribution of tidal dissipation to lunar thermal history, *Icarus*, *36*, 245–269, doi:10.1016/0019-1035(78)90109-4.
Pieters, C. M., et al. (2009), Character and spatial distribution of OH/H_2O on the surface of the Moon seen by M3 on Chandrayaan-1, *Science*, *326*, 568–572, doi:10.1126/science.1178658.

Pike, R. J. (1974), Depth/diameter relations of fresh lunar craters: Revision from spacecraft data, *Geophys. Res. Lett.*, *1*(7), 291–294, doi:10.1029/GL001i007p00291.

Pike, R. J. (1977), Apparent depth/apparent diameter relation for lunar craters, *Proc. Lunar Sci. Conf.*, *8th*, 3427–3436.

Robie, R. A., B. S. Hemingway, and W. H. Wilson (1970), Specific heats of lunar surface materials from 90 to 350 K, *Science*, *167*, 749–750.

Sackmann, I. J., A. I. Boothroyd, and K. E. Kraemer (1993), Our Sun. III. Present and future, *Astrophys. J.*, *418*, 457–468, doi:10.1086/173407.

Schorghofer, N. (2010), Fast numerical method for growth and retreat of subsurface ice on Mars, *Icarus*, *208*, 598–607, doi:10.1016/j.icarus.2010.03.022.

Schorghofer, N., and O. Aharonson (2005), Stability and exchange of subsurface ice on Mars, *J. Geophys. Res.*, *110*, E05003, doi:10.1029/2004JE002350.

Schorghofer, N., and G. J. Taylor (2007), Subsurface migration of H_2O at the lunar poles, *J. Geophys. Res.*, *112*, E02010, doi:10.1029/2006JE002779.

Simpson, R. A., and G. L. Tyler (1999), Reanalysis of Clementine bistatic radar data from the lunar south pole, *J. Geophys. Res.*, *104*, 3845–3862, doi:10.1029/1998JE900038.

Slade, M. J., B. J. Butler, and D. O. Muhleman (1992), Mercury radar imaging: Evidence for polar ice, *Science*, *258*, 635–640, doi:10.1126/science.258.5082.635.

Spudis, P. D., B. Bussey, J. Plescia, J. Josset, and S. Beauvivre (2008), Geology of Shackleton crater and the south pole of the Moon, *Geophys. Res. Lett.*, *35*, L14201, doi:10.1029/2008GL034468.

Spudis, P. D., et al. (2010), Initial results for the north pole of the Moon from Mini-SAR, Chandrayaan-1 mission, *Geophys. Res. Lett.*, *37*, L06204, doi:10.1029/2009GL042259.

Stacy, N. J. S., D. B. Campbell, and P. G. Ford (1997), Arecibo radar mapping of the lunar poles, *Science*, *276*, 1527–1530, doi:10.1126/science.276.5318.1527.

Sunshine, J. M., T. L. Farnham, L. M. Feaga, O. Groussin, F. Merlin, R. Milliken, and M. F. A'Hearn (2009), Temporal and spatial variability of lunar hydration as observed by the Deep Impact spacecraft, *Science*, *326*, 565–568, doi:10.1126/science.1179788.

Svitek, T. (1992), Martian water frost: Control of global distribution by small-scale processes, Ph.D. thesis, Calif. Inst. of Technol., Pasadena.

Touma, J., and J. Wisdom (1994), Evolution of the Earth-Moon system, *Astron. J.*, *108*, 1943–1961, doi:10.1086/117209.

Urey, H. C. (1952), *The Planets, Their Origin and Development*, Yale Univ. Press, New Haven, Conn.

Vasavada, A. R., D. A. Paige, and S. E. Wood (1999), Near-surface temperatures on Mercury and the Moon and the stability of polar ice deposits, *Icarus*, *141*, 179–193, doi:10.1006/icar.1999.6175.

Vondrak, R. R., and D. H. Crider (2003), Ice and the lunar poles, *Am. Sci.*, *91*, 322–329.

Ward, W. R. (1973), Large-scale variations in the obliquity of Mars, *Science*, *181*, 260–262.

Ward, W. R. (1974), Climatic variations on Mars: 1. Astronomical theory of insolation, *J. Geophys. Res.*, *79*, 3375–3386.

Ward, W. R. (1975), Past orientation of the lunar spin axis, *Science*, *189*, 377–379, doi:10.1126/science.189.4200.377.

Ward, W. R. (1992), Long-term orbital and spin dynamics of Mars, in *Mars*, edited by H. H. Kieffer et al., pp. 298–320, Univ. of Ariz. Press, Tucson.

Warren, P. H., and K. L. Rasmussen (1987), Megaregolith insulation, internal temperatures, and bulk uranium content of the Moon, *J. Geophys. Res.*, *92*, 3453–3465.

Watson, K., B. C. Murray, and H. Brown (1961a), On the possible presence of ice on the Moon, *J. Geophys. Res.*, *66*, 1598–1600, doi:10.1029/JZ066i005p01598.

Watson, K., B. C. Murray, and H. Brown (1961b), Behavior of volatiles on the lunar surface, *J. Geophys. Res.*, *66*, 3033–3045, doi:10.1029/JZ066i009p03033.

Weiczorek, M. A., and R. J. Philips (2000), The "Procellarum KREEP Terrane": Implications for mare volcanism and lunar evolution, *J. Geophys. Res.*, *105*, 20,417–20,430.

Wisdom, J. (2006), Dynamics of the lunar spin axis, *Astron. J.*, *131*, 1864–1871, doi:10.1086/499581.

Yseboodt, M., and J. Margot (2006), Evolution of Merucy's obliquity, *Icarus*, *181*, 327–337, doi:10.1016/j.icarus.2005.11.024.

Zhang, J. A., and D. A. Paige (2009), Cold-trapped organic compounds at the poles of the Moon and Mercury: Implications for origins, *Geophys. Res. Lett.*, *36*, L16203, doi:10.1029/2009GL038614.

B. G. Bills, NASA Jet Propulsion Laboratory, 4800 Oak Grove Dr., Pasadena, CA 91109, USA. (bills@jpl.nasa.gov)

D. A. Paige and M. A. Siegler, Earth and Space Sciences, University of California, 395 Charles Young Dr. East, Los Angeles, CA 90095, USA. (dap@mars.ucla.edu; siegler@ucla.edu)